

Simulating of Erosion Modeling Using ANSYS Fluid Dynamics

by

Aimen Marrah

A thesis submitted to the School of Graduate Studies in partial fulfillment of the requirements for

the degree of

Master of Engineering

Faculty of Engineering and Applied Science

Memorial University of Newfoundland

May-2019

St. John's

Canada

Newfoundland

Abstract

The micromechanical process of solid particle erosion can be affected by a number of factors, including impact angle, flow geometry, and particle size and shape. Erosion can also be affected by fluid properties, flow conditions, and the material comprising the impact surface. Of these several different potential impacting factors, the most critical ones for initiating erosion are particle size and matter, carrier phase viscosity, pipe diameter, velocity, and total flow rate of the second phase. Three turbulence models which are heavily dependent on flow velocities and fluid properties in their environment are k-epsilon ($k-\epsilon$), k-omega ($k-\omega$) and The Shear Stress Transport Model (sst). More extreme erosion generally occurs in gas-solid flow for geometries which experience rapid alterations in flow direction (e.g., in valves and tees) because of unstable flow and local turbulence. The present study provides results from computational fluid dynamics (CFD) simulations that feature dilute water-solid flows in complex pipelines, highlighting the dynamic behavior displayed by the flows' entrained solid particles. Specifically, the impact of fluid velocities in relation to erosion location is tested on sand particles measuring 10, 70, 100 and 200 microns. For the CFD analysis testing, liquid velocities of 20, 25, 30, 35 and 40 m/s are applied. The difference is evident between velocities of 20 m/s and 40 m/s, giving an erosion rate of 1.73×10^{-4} kg/m².s and 2.11×10^{-3} kg/m².s, respectively, when the particle solid is 200 μ m. The particle solid's effect on the erosion rate at 70 μ m gives an erosion rate of 5.79×10^{-4} kg/m².s, while the particle solid's effect at a 100 μ m gives an erosion rate of 8.03×10^{-4} kg/m².s when the velocity is 40 m/s. Data on both size and positioning of the incidence of erosion can be utilized when assessing vulnerability to erosion in arc areas (i.e., post-inlet and elbows).

In the oil and gas industry, issues around solid particle erosion and increasing erosion rates are ongoing challenges. Numerous factors come into play when trying to resolve these problems, such as the shape and size of the particles causing the erosion, and the ductility of the pipelines carrying them. As investigated in the literature, these flows can come into contact with affected surfaces at different velocities and angles. Numerical and experimental research indicates that in slow flows of phases in dense gas or liquid (e.g., slurry transport), particle impact angles tend to be so narrow that they are difficult to test. The present research study examines erosion rates in relation to primary and secondary phase flows. In order to simulate four-phase flows in a pipeline with an arc and two bends under the impact of solid/liquid particle-initiated erosion, the CFD (computational fluid dynamics) code ANSYS FLUENT is used. The simulations in this work measure fluid velocities and erosion rates/locations for 200-micron sand particles, applying liquid velocities measuring 20, 25, 30, 35 and 40 m/s in CFD-based tests. The results show that if ethane exerts the primary phase impacts with 200 microns of flow material, the erosion rate is $9.760 \times 10^{-3} \text{ kg/m}^2 \cdot \text{s}$ at speeds of $\sim 40 \text{ m/s}$. However, if methane comprises the carrier fluid with 200 microns of flow material, the erosion rate is $1.006 \times 10^{-2} \text{ kg/m}^2 \cdot \text{s}$ at sine speeds of $\sim 40 \text{ m/s}$. The present study also models how the flow particles affect the carrier fluid (e.g., methane, water, ethane), applying both one-way and full coupling. In addition, the turbulence effect exerted in a medium by the particle dispersion force against particles is examined in detail. Finally, the primary and secondary phases' impact parameters are determined in relation to frequency and speed of impact on outer wall bends. Any interactional force occurring between the particles and the carrier fluid has been considered as a measure of VOF (volume of fluid) momentum transfer.

Acknowledgments

Many people have assisted, both directly and indirectly, in the writing of this thesis. I am grateful to the Libyan Ministry of Higher Education, through the Canadian Bureau for International Education (CBIE), for their financial support.

I also extend my gratitude to Dr. John Shirokoff, my supervisor, and Dr. Mohammed Azizur Rahman, my co-supervisor, both of whom were instrumental in helping me formulate the basis for this study and bring this work to a successful conclusion.

I am thankful for their encouragement and guidance and consider them to be cherished friends for life. Additionally, I would like to thank Mr. Tarek Shikiki, my classmate, for generously sharing with me his wealth of knowledge on my topic.

Finally, I would like to thank my parents for their loving support and my wife and children for making each and every day a happy one.

Table of Contents

Abstract.....	i
Acknowledgments.....	iii
List of Figures	vii
Nomenclature	x
Chapter 1.....	1
1.1. Introduction	1
1.1.1. Definition of CFD.....	1
1.1.2. CFD advantages.....	2
1.1.3. CFD code functioning	3
1.2. Objective	7
1.3. Organization of the Thesis	7
Chapter 2.....	8
2.1. Literature review.....	8
2.1.1. Erosion in pipes.....	8
2.2. Solid Particle Erosion	8
2.3. Mechanisms underlying solid particle erosion	9
2.4. Anticipating and preventing solid particle erosion.....	10
2.4.1. Particle features.....	10
2.4.1.1. Shape characteristic.....	10
2.4.1.2. Size characteristic.	11
2.5. Methods for managing erosion	11
2.5.1. Production rate decrease	11

2.5.2. Pipework design.....	12
2.5.3. Separation and exclusion of sand.....	12
2.5.4. Sand production estimation and measurement.....	13
Chapter 3 Investigation of erosion in intricate pipelines with bends using CFD simulations	14
Abstract.....	14
Keywords.....	15
3.1. Introduction	15
3.2. Validation	18
3.3. Geometry and Meshing	19
3.4. Turbulence Model.....	22
3.5. Erosion model	23
3.5. Results and discussion	26
Chapter 4 Four-phase flow investigation of erosion in intricate pipelines with bends using CFD simulations.....	35
Abstract.....	35
Keywords.....	36
4.1. Introduction	36
4.2. Geometry and meshing	38
4.3. Discrete phase model	40
4.3.1. Volume Fraction Equation	42
4.3.2. Implicit Formulation.....	43
4.3.3. Explicit Formulation	44
4.3.4. Erosion Rate	45
4.4. Boundary conditions:.....	46

4.5. Results and discussion	47
Conclusions	55
References	56

List of Figures

Fig. 1. Shows particle damage in wall of pipe	11
Fig. 2. Validation at a velocity of 50 (m/s) using different particle solids.....	18
Fig. 3. Validation at different velocities using particle solids of 300 (μm).....	19
Fig. 4. Geometry in ANSYS and mash.....	20
Fig. 5. Maximum layers in ANSYS.....	21
Fig. 6. Comparison between three different equation turbulence models, with erosion rates for a velocity of 40 (m/s) and a particle size of 200 (μm).....	25
Fig. 7. Effect of element number on erosion rate.	26
Fig. 8. Distribution of erosion rates for bends at different inlet flow rates at 200 (μm).....	27
Fig. 9. Erosion rate for bends at different inlet flow rates at 100 (μm) and different velocities. .	27
Fig. 10. Erosion rate for bends at different inlet flow rates at 70 (μm).....	28
Fig. 11. Erosion rates for bends at different inlet flow rates at 10 (μm).....	28
Fig. 12. Deformation for three different diameters of pipes at a velocity of 40 (m/s).....	29
Fig. 13. Comparison of erosion rate per impact particle against the particle diameter and inlet flow velocity for larger inlet velocities of 20, 25, 30, 35 and 40 (m/s).	30
Fig. 14. Comparison of erosion rates at different velocities and solid particle diameters 10, 70, 100 and 200 (μm).....	31
Fig. 15. The effect of flow rates on erosion at velocities of 20 and 40 (m/s).	32
Fig. 16. Effect of solid particle density on erosion rates at different velocities 200 (μm).	32
Fig. 17. Effect of pipe diameter on erosion rates at a velocity of 40m/s and particle size of 200 (μm).....	33
Fig. 18. Effect of viscosity on erosion rates at a velocity of 40m/s and particle size of 200 (μm).	34
Fig. 19 Geometry and mesh in ANSYS.....	40
Fig. 20 Cut in the pipeline showing detail of mesh	40
Fig. 21. Distribution of erosion rates for bends when the primary phase is water at different inlet flow rates at 200 (μm).....	47
Fig. 22. Distribution of erosion rates for bends when the primary phase is Methane at different inlet flow rates at 200 (μm).....	48

Fig. 23. Distribution of erosion rates for bends when the primary phase is Ethane at different inlet flow rates at 200 (μm)..... 49

Fig. 24. Comparison of erosion rates for different solid particles and primary phase flow rates. 49

Fig. 25. Effect of pipe diameter on erosion rates at a velocity of 40 m/s and particle size of 200 (μm)..... 53

List of Tables

Table 1. DETAILS OF MESH.....	20
Table 2. BAROMETERS AND INFORMATION FOR THE SIMULATION	24
Table 3. DETAILS OF MESH.....	39
Table 4. BAROMETERS AND INFORMATION FOR THE SIMULATION	46

Nomenclature

Name	Symbols
Erosion rate	FR
Brinell hardness	B
Particle shape coefficient	F_s
Function of particle diameter	$C(d_p)$
The impact angle of the particle path with the wall face	a
Function of impact angle	$f(a)$
The relative particle velocity	v
Function of relative particle velocity	$b(v)$
The area of the cell face at the wall	A_{face}
Represents the generation of turbulence kinetic energy due to the mean velocity gradients	G_k
The generation of turbulence kinetic energy due to buoyancy	G_b
represents the contribution of the fluctuating dilatation in compressible turbulence to the overall dissipation rate	Y_M
the turbulent Prandtl numbers for K	$\sigma_K, \sigma_\varepsilon$

Constants	$C_{1\varepsilon}, C_{2\varepsilon}, C_{3\varepsilon}$
Default values	C, f, b
The mass transfer from phase	m_{qp}
Index for current time step	$n + 1$
Index for previous time step	n
Cell value of volume fraction at time step n+1	a_q^{n+1}
Cell value of volume fraction at time step n	a_q^n
Face value	$a_{q,f}^{n+1}$
Volume flux through the face at time step n+1	U_f^{n+1}
Cell volume	V

Chapter 1

1.1. Introduction

1.1.1. Definition of CFD

We can generally define computational fluid dynamics (CFD) as a method which uses computer-based simulations to analyze systems that include heat transfer, fluid flows, and chemical reactions. CFD can be utilized in a broad spectrum of engineering and other applications, some of which are listed below:

- Chemical process engineering: Used in separation and mixing processes, including polymer molding.
- Electrical and electronic engineering: Used for equipment cooling (e.g., microcircuits).
- Marine engineering: Used in off-shore structural loads.
- Environmental engineering: Used for effluent and pollutant distribution.
- Biomedical engineering: Used in technology involving arterial and venous blood flow.
- External and internal environment of buildings: Used in ventilation, heating and wind loading.
- Turbomachinery: Used for diffusers, interior rotating passage flows, etc.
- Power plant: Used for gas turbine and internal combustion engines.
- Ship hydrodynamics.
- Hydrology and oceanography: Used for river, ocean, and other flows.
- Meteorology: Used in predicting weather and climate.
- Vehicle and aircraft aerodynamics: Used for calculating lift and drag.

CFD methods have been applied in both industrial and non-industrial uses since the early 1960s. For instance, the aerospace industry uses CFD during the Research and Development (R&D) stages of the design of jet engines and aircraft, as well as in their manufacturing stage.

Other applications of CFD include gas turbine combustion chambers, furnaces, and combustion engines. CFD is also being used by motor vehicle manufacturers for studying in-car environments, air flows under the bonnet, and drag forces. From these applications, it is clear that CFD has become an important aspect of the industrial design and manufacturing process [1].

Over the years, CFD has strived to achieve the same abilities as similar tools in the computer-aided engineering (CAE) field. Despite this ambition, the intricate behavior inherent in the CFD method has prevented it from being able to provide a sufficiently thorough and/or affordable fluid flow characterization. This has changed recently, however, with the development of more economical computer hardware that is both high-performance and features more user-friendly formats, giving the CFD approach a new chance to be adopted for mainstream use [1].

1.1.2. CFD advantages

Compared to strategies that are more experiment-based, CFD features a number of advantages in relation to the design of fluid systems. Some of the main advantages are listed below:

- Major decrease in price and turnaround time for designs.
- Capable of testing the viability of different types of systems (such as large systems) that controlled experiments cannot investigate for reasons of practicality.
- Capable of testing the viability of systems beyond the scope of normal operating conditions and in dangerous circumstances such as accidents and explosions.
- Virtually limitless degree of detail in relation to testing outcomes.

A major improvement in CFD has been the reduction in costs associated with the method. Experiments require expenses (employees, facilities, etc.) that are either not required or only negligible with CFD. Moreover, CFD codes are able to provide sizeable results volumes at a

fraction of the cost of live experiments, and can employ parametric studies as a means to optimize the performance of the equipment used.

The next section reviews CFD code structure in general and investigates how individual building blocks impact design, performance and cost. Additionally, we look at the skills that are needed for running the codes as well as communicating results, and suggest that the lack of appropriately trained workers could, over the years, have been more of a hindrance to the adoption of CFD than its cost or the availability of its components [1].

1.1.3. CFD code functioning

The codes for CFD are geared towards numerical algorithms which address fluid flow issues. Therefore, as a means to ensure ease of accessibility for solving power, CFD packets feature user interfaces that clearly show input problem parameters along with the solving process and the end results. The three key parts of the codes are the pre-processor, the post-processor and the solver. The next three sections present a short summary of each of these parts [1].

1.1.3.1. Pre-processor

In CFD programs, pre-processing comprises the flow problem's input by employing a user-friendly interface. The input is then transformed to make it appropriate for the solver to use. There are several activities specific to the pre-processing stage. The main ones are listed below:

- The region of interest's geometry is defined: This is considered the computational domain.
- During grid generation, the computational domain is then divided into several sub-domains which are smaller than the original domain and do not overlap. The division orders the cells (also known as 'elements' or 'control volumes') into a formation that is similar to a grid or mesh pattern.

- The chemical and/or physical elements that need to be transformed are then selected.
- Fluid properties are defined.
- Suitable boundary conditions for cells that impact domain boundaries are designated.

A flow problem's solution, which includes aspects of temperature, pressure, velocity, etc., is based on observing the nodes within the cells. In fact, the CFD solution's relevancy is determined through the cell count of the grid, with a higher amount of cells indicating a higher degree of accuracy. A finer grid can, however, be costly both in terms of required calculation time and computer hardware. The best option has been shown to be mesh that is non-uniform in character, featuring finer meshing for regions of greater variations and larger meshing for areas that see few variations. To that end, R&D departments are looking to develop codes for CFD that feature a type of adaptive or self-adaptive mesh. However, commercially available technology still relies on individual CFD users for grid designs that are reasonably accurate while also being relatively inexpensive and fast.

Over half the time allotted to CFD projects must be spent on defining domain geometry and subsequent grid generation. However, productivity has recently been improved by having all major codes include a distinct CFD type of interface for importing data out of mesh generators as well as surface modelers (e.g., PATRAN and I-DEAS). Additionally, modern pre-processors not only permit users to access libraries on the material properties of common fluids, they also provide a facility for exploring specific chemical/physical process models, such as combustion models, radiative heat transfer, and turbulence models. These are included with the primary equations for fluid flow [1].

1.1.3.2. Post-processor

The post-processor field, similar to pre-processing, has seen radical improvements over the past few decades. As a result, CFD programs now come with enhanced visualization and graphics capabilities, such as:

- Surface plots for 2D and 3D
- Grid display
- Domain geometry
- Postscript output in color
- Plots featuring shaded contour and lines
- Vector plots
- Manipulation of view (for scaling, rotation, etc.)
- Particle tracking
- Animation

Moreover, the codes now feature accurate alph-numeric output as well as data export facilities, enabling external changes to be made. In particular, the graphics enhancements in CFD codes have enabled non-specialists to use the programs [1].

1.1.3.3. Solver

Numerical solution approaches can be divided into three main categories of spectral methods, finite element, and finite difference. This study looks at the finite difference category of finite volume method, which is a key component in popular CFD codes such as FLUENT, CFX/ANSYS, STAR-CD and PHOENICS. A typical numerical algorithm follows certain steps, more or less in order:

- The first step involves integrating fluid flow governing equations for the domain's finite control volumes.

- The next step involves converting the integral equations that result into an algebraic system of equations. This step is known as discretization.
- The third step involves an iterative approach towards finding the algebraic equations' solutions.

By integrating the control volumes (first step), the finite volume approach is shown to be unique compared to other CFD methods. Specifically, the statements which result from the integration reveal precise conservation in the relevant properties for every finite size cell. The obvious connection between the principle of physical conservation and the numerical algorithm makes the finite volume approach very user-friendly compared to other strategies such as spectral and finite element. So, for instance, in finite control volume, the conservation of general flow variables for ϕ , the velocity component is easily expressed as the balance of a range of different processes which either reduce or enhance it, as follows:

$$\left[\begin{array}{l} \text{Rate of change} \\ \text{of } \Phi \text{ in the control} \\ \text{volume with respect} \\ \text{to time} \end{array} \right] = \left[\begin{array}{l} \text{Net rate of} \\ \text{increase of } f \text{ due} \\ \text{to conectionl in to} \\ \text{the control volume} \end{array} \right] + \left[\begin{array}{l} \text{Net rate of} \\ \text{increase of } f \text{ due} \\ \text{to diffusion into the} \\ \text{control volume} \end{array} \right] + \left[\begin{array}{l} \text{Net rate of} \\ \text{creation of } f \\ \text{inside the control} \\ \text{volume} \end{array} \right]$$

We can find in CFD codes discretisation strategies that are applicable for use in crucial transport aspects such as *diffusion*, which is transport caused by changes in ϕ occurring between points, and convection, which is transport caused by fluid flow. These strategies are also useful in source terms related to the development or termination of ϕ and in change rates that are time contingent. Because the physical phenomena underlying the scenarios tend to be non-linear and relatively complicated, a solution which is iterative is a necessity. Solutions related to velocity and pressure can be optimized by using SIMPLE algorithm or TDMA (tri-diagonal matrix algorithm)

line-by-line solver for algebraic equations. The Gauss-Seidel approach, which uses conjugate gradient method along with multigrid accelerators, is also suitable for iterative solutions [1].

1.2. Objective

The primary objective of the present thesis work is to propose numerical simulations and their validations for experimental data in order to develop a knowledge base that can be applied to the erosion mode for multi-phase flow processes in CFD. Two types of multi-phase models in ANSYS CFD software are studied to measure both their advantages and disadvantages in applications related to erosion rates. A supplementary aim of this work is developing a CFD model which can be applied to pipeline research, especially with regard to annular pipe flows of multi-phase slug fluids. The proposed CFD model will be tested for its validity in two-phase end-water flows for complex pipelines.

1.3. Organization of the Thesis

This thesis is written in manuscript format. Outline of each chapter is explained below:

Chapter 1 A brief introduction of CFD.

Chapter 2 Literature review of erosion rate modeling.

Chapter 3 Investigation of erosion in intricate pipelines with bends using CFD simulations.

Chapter 4 Four-phase flow investigation of erosion in intricate pipelines with bends using CFD simulations.

Chapter 5 Conclusions.

Chapter 2

2.1. Literature review

The literature on the transportation of oil and gas includes a significant amount of information about CO₂/H₂S, highlighting in particular the wear and tear on pipelines that takes the form of erosion [2].

2.1.1. Erosion in pipes

The oil and gas industry has a lengthy experience with corrosions caused by solid particles in pipelines. A few studies have investigated the occurrence of erosion as well as corrosion, but given the global expansion of the oil and gas industry, the research area requires further work [2].

2.2. Solid Particle Erosion

In the solid particle erosion process which takes place in the oil and gas industry, material either erodes or is removed from a pipe surface. Both the eroding substance and the substance being eroded suffer reductions in form and content. Fluid flows can also cause erosion-related reductions to the surface material of pipelines [2], [3]. The erosion is greatest when the substance being transferred contains a corrosive or corrosion-inducing material [4]. Despite the long-term occurrence of erosion in pipelines, it remains a major issue in the oil and gas industry [5, 10].

Erosion occurs as a process rather than as a one-off event. In other words, pipeline erosion occurs over a sequential time period, leading to substances being removed from the pipe. Erosion can take the form of plastic deformations or brittle fractures in the pipes caused by various materials impacting the steel [2]. Several studies have investigated the process of erosion-related corrosion, looking at aspects such as failure analysis and erosion-corrosion behaviors. The procedures involved include examination of scanning electron microstructure; electrochemical

methods; visual examination; and computational fluid dynamics (CFD). The present investigation looks at CFD simulation using ANSYS software [4]. CFD simulations indicate that a strong turbulent flow develops if the opening comprises only a small inlet. The turbulent flow then leads to material erosion in the pipes. Furthermore, crack initiation generally depends on turbulence intensity and abrupt changes in pressure [4]. The following section presents an overview of modeling for solid particle erosion in pipelines and oil and gas wells.

2.3. Mechanisms underlying solid particle erosion

As soon as a particle impacts a surface, however slightly, the surface is impacted and thus scarred. The actual shape of the impact scar is determined by a number of factors, ranging from the ‘attack angle’ to the type and size of the material. Of the many factors involved, surface ductility appears to be one of the most important [5].

Parsi et al [5]. investigated the effect of micro-geometry on the erosion process, proposing that micro-cutting is the main cause for all types of erosion. So, for instance, if a particle consistently impacts the same surface at a specific angle, other particles serve to enlarge that crater by piling materials in the area surrounding the crater. The materials then experience constant removal from the crater edge via the erosion “attack”. However, the model proposed in [5] fails to measure the scale of erosion events impacting the inside portion; the model also does not fare well in relation to other experiments and data. The researchers suggested that pipeline surfaces need to be reinforced to prevent severe erosion events [5].

Additionally, they proposed the existence of “platelets”, which are shallow craters caused by particles impinging on pipeline surfaces [5]. During the erosion process, due to heat impacting the surface of the substance (as well as below the surface), hardening occurs. Hence, in instances that are conducive to the formation of platelets, there is also increased erosion either due to the

brittleness of the material or crack initiation [5]. When a brittle surface is impinged by a particle, radial cracking occurs; these cracks develop further due to additional erosion and can ultimately form divisions in the material [5].

2.4. Anticipating and preventing solid particle erosion

A number of different factors contribute to pipeline erosion, the main ones of which are the physical features of the material, such as type, hardness, density, shape and size. At the same time, ratio equations vary according to the different features of the particles (e.g., information and data on impingement, the relation of the surface material to surface mass loss, etc.). Erosion rates can be based on pipeline thickness and/or mass loss of piping surface, while function time may be assumed as miles per annum, millimeter per annum, kg/hour, etc. Different researchers adopt different approaches according to their data and circumstances [5].

2.4.1. Particle features

Solid particle erosion is impacted by a variety of features, including size, shape, hardness, density, material type, etc., of both the materials being impinged and the eroding substances. In order to determine accurate outcomes, the particle features and characteristics need to be thoroughly examined [5].

2.4.1.1. Shape characteristic.

The shape of a particle can determine the extent of the erosion. So, for instance, particles that are characterized as sharp can have a significant effect on erosion scale, depth, and duration. In [5], the researchers tested both spherical and sharp-angled particles, finding that the sharp particles resulted in a four-fold increase in erosion effects over the spherical particles. This outcome indicates the interrelation of particle shape and angularity to erosion [5], [6]. Hence, the characteristic of shape was added to erosion ratio equations [5].

2.4.1.2. Size characteristic.

The size of a particle also impacts erosion potential. In general, larger particles have greater amounts of kinetic energy while impinging pipeline materials at similar speeds as smaller particles. In the data, the function of erosion ratio is assumed as the eroded materials' mass / impinged materials' mass. However, this ratio does not appear to have an influence on particles exceeding 100 μm [5]. In one experiment, the erosion influence of sand on cast iron was investigated using angles of approximately 30° and 75° [1], [5]. As shown in Fig. 2, the velocity of the carrier fluid was 3.63 m/s and the sand concentrations were 20 wt %. The results of the experiment indicated a clear linear association, showing the particle speed as being unsteady and changeable in liquid flows [5].

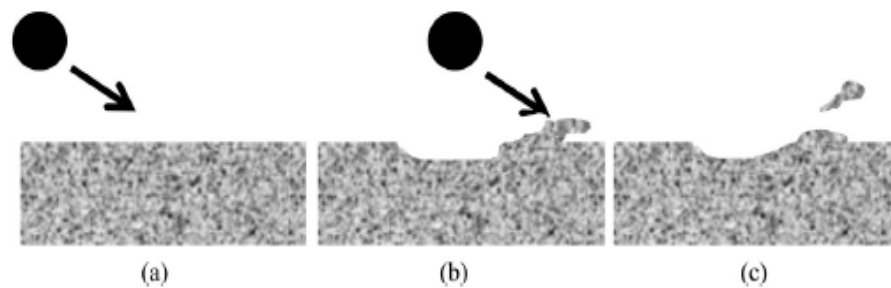


Fig.2. shows particle damage in wall of pipe

2.5. Methods for managing erosion

Several different kinds of erosion management approaches have been proposed to anticipate, measure and prevent erosion. The most common approaches are briefly explained in the following sections.

2.5.1. Production rate decrease

Reducing production rates will also cause both the speeds in the pipeline and the production of sand to be reduced. Such reductions, however, will likely increase costs, as production time will be expanded [5].

2.5.2. Pipework design

Ideally, well-designed pipelines should have the capacity to reduce flow speeds and prevent unnecessary alterations to flow caused by devices such as valves, constrictions or elbows. To this end, pipeline design could incorporate blind tees and bore valves as a means to lower pipe erosion rates. Furthermore, because slug flows can also cause significant damage to pipes, pipeline design should include sufficient use of drainage. Another aspect of design involves wall thickness. Thicker walls, though increasing costs slightly, could help prevent deep cracks in shallow materials from destroying the infrastructure [5].

2.5.3. Separation and exclusion of sand

Inhibiting the introduction of sand to pipelines in oil and gas sites is crucial. However, preventing the intrusion of sand can be difficult, so gravel packs and downhole sand screens are used in most pipeline infrastructures to keep too much sand from entering the systems. Sand has particularly become a problem in newer wells due to size allowances which permit larger particles to gain system access. Far from being merely a nuisance, sand decreases well productivity because the sand screens increase the unsteadiness of the flow. Therefore, sand screens and the flow have to be equally balanced. Moreover, sand screens alone are insufficient for preventing pipeline erosion from sand [5].

The tools most commonly used to deal with the presence of sand in pipelines include hydroclones and desanders. These and other kinds of separation devices help to reduce (though not stop) erosion levels; they can also, unfortunately, be relatively ineffective downhole, depending on the site [5].

2.5.4. Sand production estimation and measurement

Like separators, collectors are used in pipelines to deal with the negative impact of sand. Sand production is typically dependent on geology and location. It can be determined that if certain wells in a certain area are known to produce large amounts of sand, it is likely that wells in the vicinity will also produce similar amounts of sand. In these instances, monitors can be employed to keep track of any erosion occurring or anticipated to occur in the pipelines. Sand monitoring equipment is usually placed in pipe tubings located downhole. The two main tools used in monitoring are probes and non-intrusive instruments which are attached to pipework [5]. The usefulness of monitoring tools varies according to location and extent of usage [5].

Chapter 3 Investigation of erosion in intricate pipelines with bends using CFD simulations

Aimen Marrah, Mohamed Aizzur Rahman, John Shirokoff.

Abstract: — The micromechanical process of solid particle erosion can be affected by a number of factors, including impact angle, flow geometry, and particle size and shape. Erosion can also be affected by fluid properties, flow conditions, and the material comprising the impact surface. Of these several different potential impacting factors, the most critical ones for initiating erosion are particle size and matter, carrier phase viscosity, pipe diameter, velocity, and total flow rate of the second phase. Three turbulence models which are heavily dependent on flow velocities and fluid properties in their environment are k-epsilon ($k-\epsilon$), k-omega ($k-\omega$) and (sst). More extreme erosion generally occurs in gas-solid flow for geometries which experience rapid alterations in flow direction (e.g., in valves and tees) because of unstable flow and local turbulence. The present study provides results from computational fluid dynamics (CFD) simulations that feature dilute water-solid flows in complex pipelines, highlighting the dynamic behavior displayed by the flows' entrained solid particles. Specifically, the impact of fluid velocities in relation to erosion location is tested on sand particles measuring 10, 70, 100 and 200 microns. For the CFD analysis testing, liquid velocities of 20, 25, 30, 35 and 40 m/s are applied. The difference is evident between velocities of (20 m/s) and (40 m/s), giving an erosion rate of 1.73×10^{-4} kg/m².s and 2.11×10^{-3} kg/m².s, respectively, when the particle solid is 200 μ m. The particle solid's effect on the erosion rate at 70 μ m gives an erosion rate of 5.79×10^{-4} kg/m².s, while the particle solid's effect at a 100 μ m gives an erosion rate of 8.03×10^{-4} kg/m².s when the velocity is 40 m/s. Data on both size

and positioning of the incidence of erosion can be utilized when assessing vulnerability to erosion in arc areas (i.e., post-inlet and elbows).

Keywords: Erosion, Mesh, Solid Partible, CFD

3.1. Introduction

In light of restrictions regarding equipment installation, bends are often used as relief lines for bypassing immovable obstacles. However, the use of bends creates a sudden alteration in the direction of the flow, causing vibrational pipe displacement. In fact, in sizeable emissions, the compressible flow of water constantly increases in the relief line, eventually moving as fast as the speed of sound (i.e., 343 m/s). The rate of flow is problematic from a site safety perspective, as the majority of relief pipelines below the final elbow tend to be unfixed and thus prone to swinging [7]. Specifically, in bends, drops of liquid along with particles of hydrate branch off the main streamlines for carrying water, leading to pipe walls undergoing the process of particle impingement [7]–[9].

Given the enormous speed of the particles as they impact the walls, extreme erosion at the relief line elbow is usually unavoidable. Hence, this erosion, coupled with pipeline vibrations, often leads to pipeline failure, which then causes higher maintenance fees as well as issues around environmental degradation of the site. In particular, relief pipeline failures at high-sulphur gas wells could ultimately end in site destruction. Considering the high potential for such a devastating outcome, a thorough analysis is urgently required that takes into consideration both flow erosion and relief pipeline flow-induced displacement.

Flow-induced pipe displacement results from liquid flow interaction with pipeline infrastructure. To date, numerous studies have investigated the phenomenon in an attempt to envision and manage the risks and possible outcomes [7], [10]–[13]. However, very little

research has as yet been devoted to pipeline vibrations which occur downstream of bends. The issue is made even more complicated by the extreme levels of internal fluid pressure and the extreme speed of the particle-laden water that is moving through the pipelines.

Some research has been conducted related to pipeline erosion occurring at bends [14]–[19], using computational fluid dynamics (CFD) simulations for determining the extent and precise region of erosion in the elbows. Especially crucial are the properties of the carrying fluids, including particle size and content, with a number of models being designed according to test outcomes on gas flows which have solid particles and single-phase fluids [20].

Thus far, the majority of the studies have investigated incompressible flows of liquids in conditions mimicking normal or low atmospheric pressures, such as slurry transport. However, fluid flows such as particle-laden gas have the capacity to be compressible when flowing through a high-pressure pipeline. Furthermore, the speed and density of such flows can undergo severe alterations when moving through the line reaching the speed of sound (i.e., 343 m/s).

In light of the potential complications that could emerge from such flow velocities, and given that this has not yet been investigated as a causation factor in pipe vibration displacement and flow erosion, the present study looks at possible interacting influences in pipe displacement and erosion. The investigation will apply a coupling analysis to determine flow erosion and liquid/structure interactions in compressible water-particle flows along elbow pipelines. The aim of the analysis is to determine the extent and exact location for the most extreme maximum swings and erosion occurring along relief pipelines. However, because such tests are quite expensive to conduct, computational fluid dynamics will instead be used in the present study [21].

Particle flow and subsequent erosion can be a major factor in industrial, environmental and other applications, such as ventilation and conveyance systems [22]–[26], yet this phenomenon has not yet been adequately investigated for flows and erosion in relation to pipeline bends. In related research, Sun and Lu. [26] looked into the particle flow distribution and deposition behavior in 90° bends, while J. Lin et al. [27] researched the transport and deposition of nanoparticles in a rotating curved pipe. As well, Zhang et al. [28] used CFD to study near-wall and volume improvements in the prediction of particle impact on sharp bend areas, while Ke et al. in [29] studied modeling and numerical analysis in relation to solid particle erosion in curved ducts. Despite a few studies being done on particle erosion in bends, there is currently very little prediction research which focuses specifically on erosion distribution.

Recent CFD studies investigating flow-induced vibration and flow erosion have supported the efficacy of numerical methods. In light of these validations, the present research will design a CFD model that includes Fluid Structure Interaction (FSI) and Discrete Phase Model (DPM) elements. This model will then be applied to study flow erosion in bend zones of high-pressure gas relief pipelines, as well as flow-induced displacement in relief pipelines located downstream of bends. After determining the flow-field distribution for the relief pipeline's compressible particle-laden gas flow, the region where the most severe erosion and vibration-related displacement can be estimated. Next, the impact of the pipeline diameter, phase content and inlet flow-rate is explained. This paper highlights erosion status modeling in curved-wall analysis, using the results from both particle and air flow to determine erosion information relevant for standard 90-degree bends. We also analyze erosion rate behaviors that change according to particle diameter, flow rates, deflection angles, three different

equation turbulence models ($k-\epsilon$, $k-\Omega$ and SST), and inlet velocity. Numerical methods are employed to investigate the flow erosion rate on a bend in high velocity. Finally, the flow field distribution of compressible particle-laden liquid flow in a relief line is obtained to predict the location of the maximum erosion in the elbow as well as the maximum displacement of the pipe.

3.2. Validation

The steps must first be validated before being applied in real work. Sun and Lu [20] performed numerical analyses of solid particle erosion with different velocities, but their approach differs from CFD mainly in that is employed the Reynolds Stress Model (RSD), whereas CFD employs $k-\epsilon$. Additionally, there were differences in the pipeline material used. Figure 3.1 shows validation at velocity 50 m/s using a variety of particle solids diameter, while Figure 3.2 depicts validation at different velocities and particle solids of 300 μm .

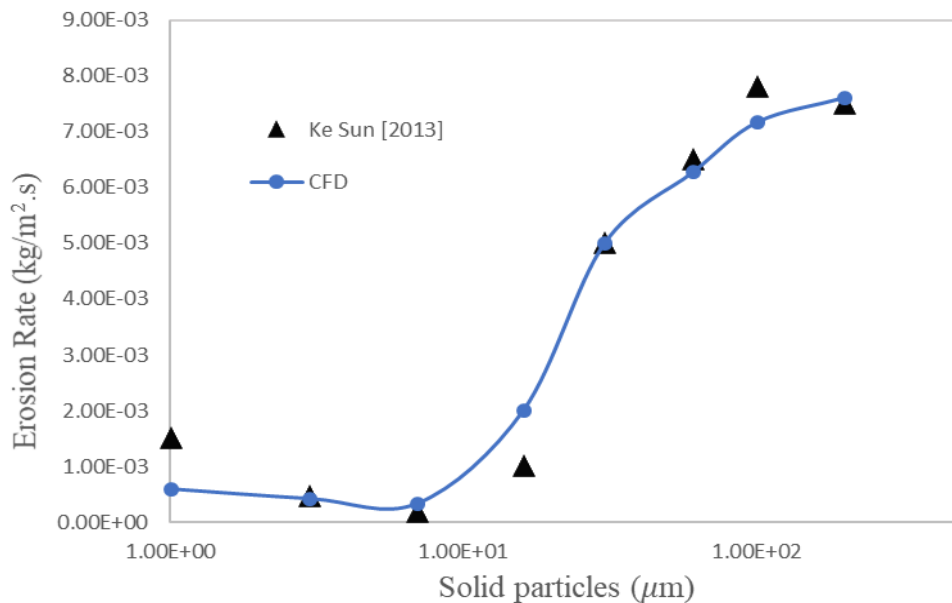


Fig. 3.1. Validation at a velocity of 50 (m/s) using different particle solids.

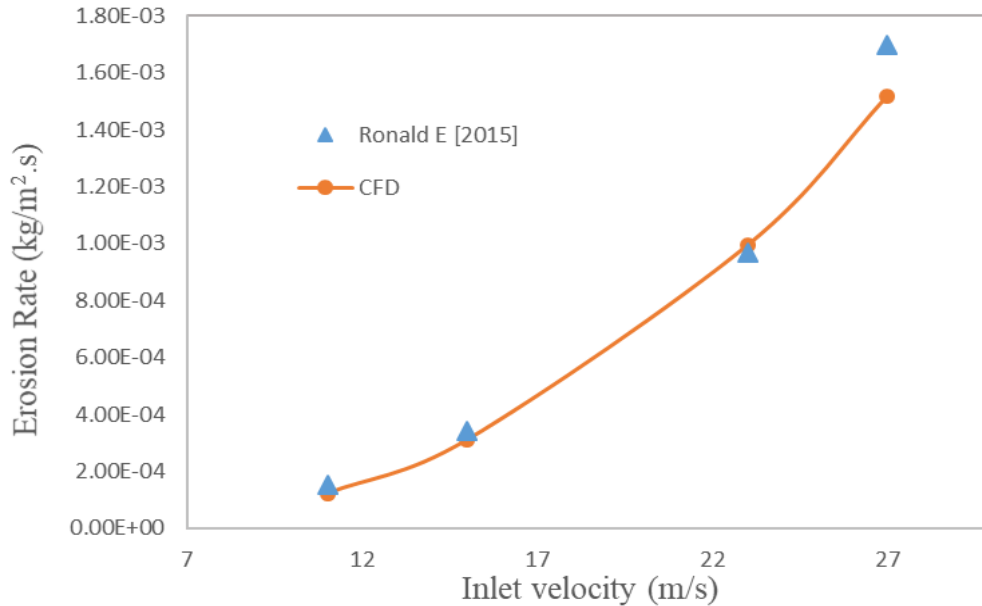


Fig. 3.2. Validation at different velocities using particle solids of 300 (μm).

3.3. Geometry and Meshing

The SOLIDWORKS software Design Modeler is tested and used to model the bean choke. The geometry is sketched in 2D and then a revolve function is employed to make the pipe 3D. Next, the geometry is imported in ANSYS to obtain the geometry mesh for the aluminum pipe (length 17 cm, diameter 4.52 cm, and three elbows at 90°). Figures 3.3 and 3.4 geometry in ANSYS, while Table 3.1 lists the mesh information.

The Directed Mesh Inflation in ANSYS Fluent was used to develop the material, demonstrating an appropriateness for simulating a two-phase flow in a horizontal pipe. Directed Mesh Inflation was chosen because of its ability to decrease both the computational time and the number of cells in comparison to alternative meshing techniques, as well as its ability to form grids parametrically in a multi-block structure. By employing the path mesh, the user can control and specify the number of divisions in the inlet cross-section, enabling the creation of quadrilateral faces. Furthermore, by applying a novel type of volume distribution, users can specify how many layers they want to have on the pipe. Figure 4 illustrates the mesh.

To generate volume mesh, hexahedral grid cells were created through the extrusion of quadrilateral faces along the length of the pipe at each layer, as shown in Figures 3.3 and 3.4. Table 3.1 provides details of the mesh grid which was most appropriate in the present case, as such a grid enables a fine cross-sectional mesh to be created without also requiring an equivalent longitudinal one.

Table 3.1. DETAILS OF MESH

Nr. of elements	153721
Nr. of nodes	67172
Element size [mm]	0.617
Maximum layers	10

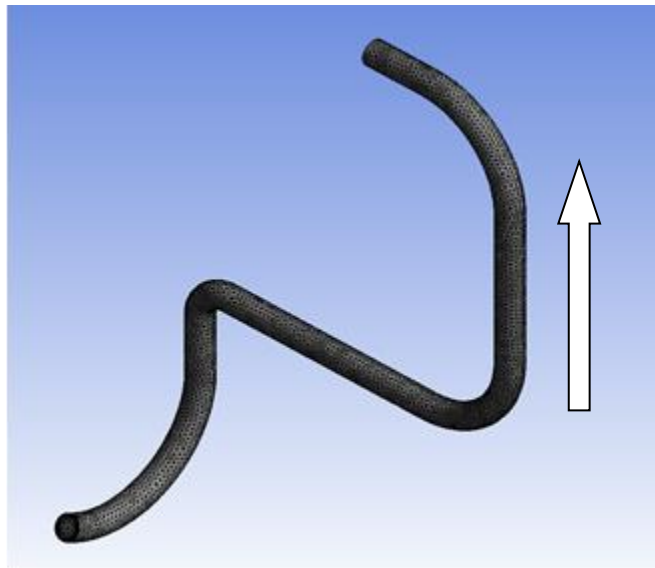


Fig. 3.3. Geometry in ANSYS and mesh.

In shifting probes in a fluid domain from a freestream flow to a wall, a non-linear reduction in velocity will be encountered until the fluid reaches zero velocity (i.e., when it reaches the wall). In CFD terms, the achievement of zero velocity is referred to as the ‘no-slip’ wall condition. In

plotting a velocity profile for the area nearest the wall, significant velocity changes occur that must be included in the CFD simulation in order to accurately factor in the gradient. Inflation layer meshing can be used here for measuring boundary layer regions in turbulent flows which are wall-bounded. However, because flow behaviors for near-wall regions are relatively complicated, they must be suitably captured to obtain valid CFD results for critical engineering data (e.g., pressure drops and points of separation) [30].

The inflation mesh, turbulence model, and flow field are all interconnected elements. To obtain a good resolution of the boundary layer, we can either resolve the layer's complete profile or reduce cell counts by applying empirical wall functions. In flows that feature heavy wall-bounded effects, effective boundary layer resolution is essential; in other types of simulations, however, it can just be cumbersome and not always necessary. Figure 3.5 below illustrates the maximum number of layers when using ANSYS [30].

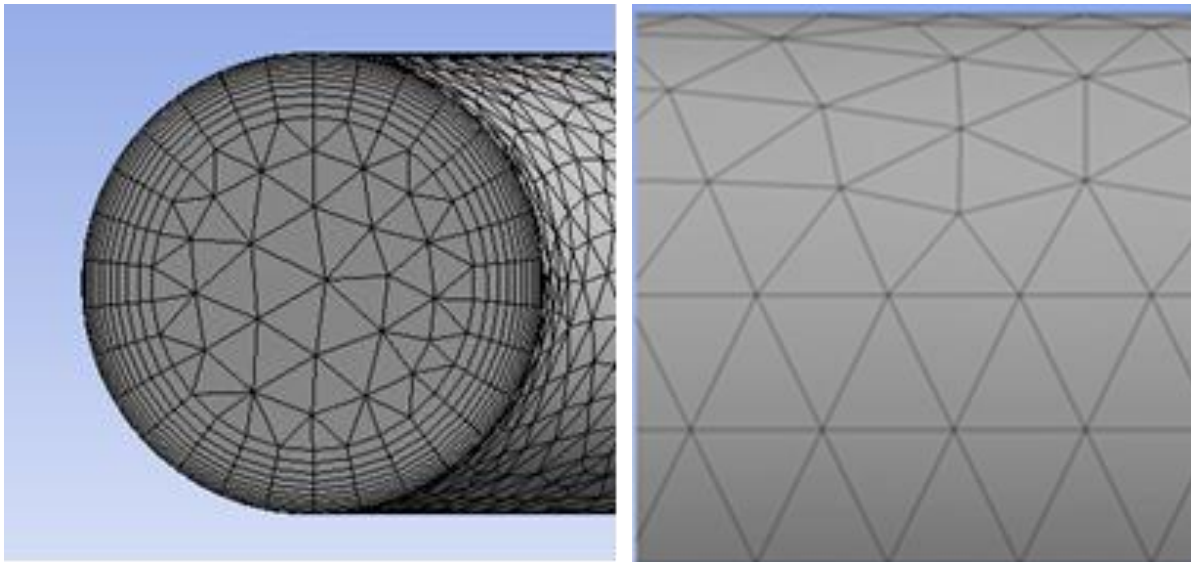


Fig. 3.4. Maximum layers in ANSYS.

3.4. Turbulence Model

By using dual-equation turbulence models, we can obtain turbulent time scales as well as turbulent lengths through the formulation of two transport equations. Launder and Spalding's ANSYS Fluent standard k- ε model has traditionally been employed in engineering flow calculations due to its relative ease of use, accuracy, and applicability across a broad range of turbulent flows, including heat transfer and industrial flow simulations. As this model is considered semi-empirical, empiricism is mainly utilized in deriving the model's equations.

The standard k- ε model uses model transport equations to obtain dissipation rate ε and turbulence kinetic energy k . Hence, the model transport equation for k can be obtained by applying the precise equation, whereas the model transport equation for ε can be determined through the application of physical reasoning. Thus, to derive the k- ε model, we can assume a fully turbulent flow but negligible molecular viscosity effects, making this k- ε model only applicable in flows which are fully turbulent. Hence, alterations are needed to improve both the model's applicability and its performance. Two model variants that use ANSYS Fluent are the k- ε model and realizable k- ε model, as formulated below [31].

$$\frac{\partial}{\partial t}(\rho k) + \frac{\partial}{\partial x_i}(\rho k u_i) = \frac{\partial}{\partial x_j} \left[\left(\mu + \frac{\mu_t}{\sigma_k} \right) \frac{\partial k}{\partial x_j} \right] + G_k + G_b - \rho \varepsilon - Y_M + S_k \quad (3.1)$$

$$\frac{\partial}{\partial t}(\rho \varepsilon) + \frac{\partial}{\partial x_i}(\rho \varepsilon u_i) = \frac{\partial}{\partial x_j} \left[\left(\mu + \frac{\mu_t}{\sigma_\varepsilon} \right) \frac{\partial \varepsilon}{\partial x_j} \right] + C_{1\varepsilon} \frac{\varepsilon}{k} (G_k + C_{3\varepsilon} G_b) - C_{2\varepsilon} \rho \frac{\varepsilon^2}{k} + S_\varepsilon \quad (3.2)$$

In the formulations, G_k depicts turbulence kinetic energy generation from mean velocity gradients; G_b indicates turbulence kinetic energy generation caused by buoyancy; Y_M refers to fluctuating dilatation contributions in compressible turbulence in relation to total dissipation rate;

$C_{1\varepsilon}$, $C_{2\varepsilon}$ and $C_{3\varepsilon}$ indicate constants; σ_k and σ_ε represent turbulent Prandtl numbers of k and ε ; and S_k and S_ε denote sources terms as defined by the users.

3.5. Erosion model

In this section, the model suggested for erosion estimation is selected, with the equation coming from the formula found experimentally, as given below:

$$R_{\text{erosion}} = \sum_{p=1}^{N_{\text{particles}}} \frac{\dot{m}_p C(d_p) f(\alpha) v^{b(v)}}{A_{\text{face}}} \quad (3.3)$$

where $C(d_p)$ is a function of particle, α is the impact angle of the particle path with the wall face, $f(\alpha)$ is a function of impact angle, v is relative particle velocity, $b(v)$ is a function of relative particle velocity, and, A_{face} is the area of the cell face at the wall.

Default values are: $C = 1.8 \times 10^{-9}$, $F = 1$ and $b = 0$ in ANSYS Fluent. We can modify formulations expressing erosion models such that they take the format of a general equation for erosion rate, as expressed in Equation 3.3. So, for instance, we can rewrite the Tulsa Angle Dependent Model [31].

$$ER = 1559B^{-0.59} F_s v^{1.73} f(\alpha) \quad (3.4)$$

as Equation 3.3 by making substitutions as follows:

$$\begin{aligned} v^{1.73} &= v^{b(v)} \\ 1559B^{-0.59} F &= C(d_p) \end{aligned}$$

where ER indicates erosion rate, B denotes Brinell hardness, and F represents the particle shape coefficient.

Table 3.2. BAROMETERS AND INFORMATION FOR THE SIMULATION

Fluent Setting	
Inlet	20, 25, 30, 35 & 40 (m/s)
Outlet	Pressure outlet
Wall	No Slip
Turbulent	k-epsilon
k-epsilon	DPM
Injection Surface	
Velocity	20, 25, 30, 35 & 40 (m/s)
Diameter	10, 70, 100 & 200 (μm)
Density	1500, 2000, 7800 & 8900 (kg/m^3)
Total Flow Rate	0.5, 1, 2, 3, & 4 (kg/s)
Discrete Phase	
Velocity	20, 25, 30, 35 & 40 (m/s)
Density	998.2 (kg/m^3)
Viscosity	0.2, 1, 5, 25 and 125 ($\text{kg}/\text{m}\cdot\text{s}$)
Pipes Information	
Length	177 (cm)
Diameter	4.52, 6.52, 8.52 & 9.52 (cm)
Material	Aluminum

k-epsilon ($k-\epsilon$), k-omega ($k-\omega$) and (sst) turbulence are the most common models used in CFD to simulate mean flow characteristics for turbulent flow conditions. The $k-\epsilon$ turbulence model

offers closer data than the others for maximum erosion and distribution along the pipe, but the sst and k- ω models show good prediction as well, as can be seen in Figure 3.5.

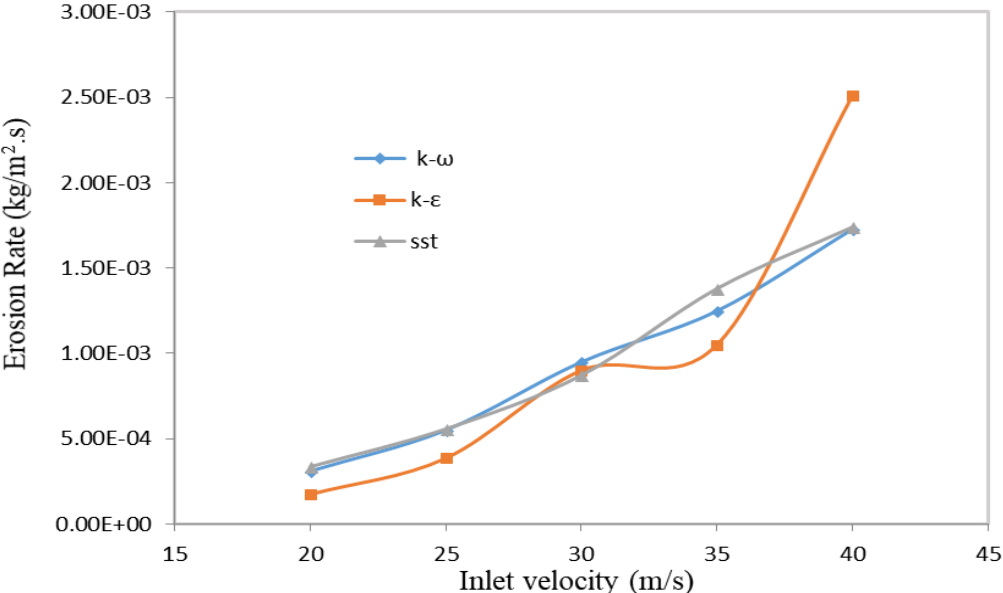


Fig.3.5. Comparison between three different equation turbulence models, with erosion rates for a velocity of 40 (m/s) and a particle size of 200 (μm).

Independent mesh numbers are shown in Figure 3.6, with element numbers ranging between 0.5 million and 2 million. The 1 million element line provides almost the same erosion rate as 2 million, which is slightly more than the 1.5 million element line. Although there are slight differences in erosion rates at velocities of 20, 25, 30 and 35 m/s, the difference becomes clear at a velocity of 40 m/s.

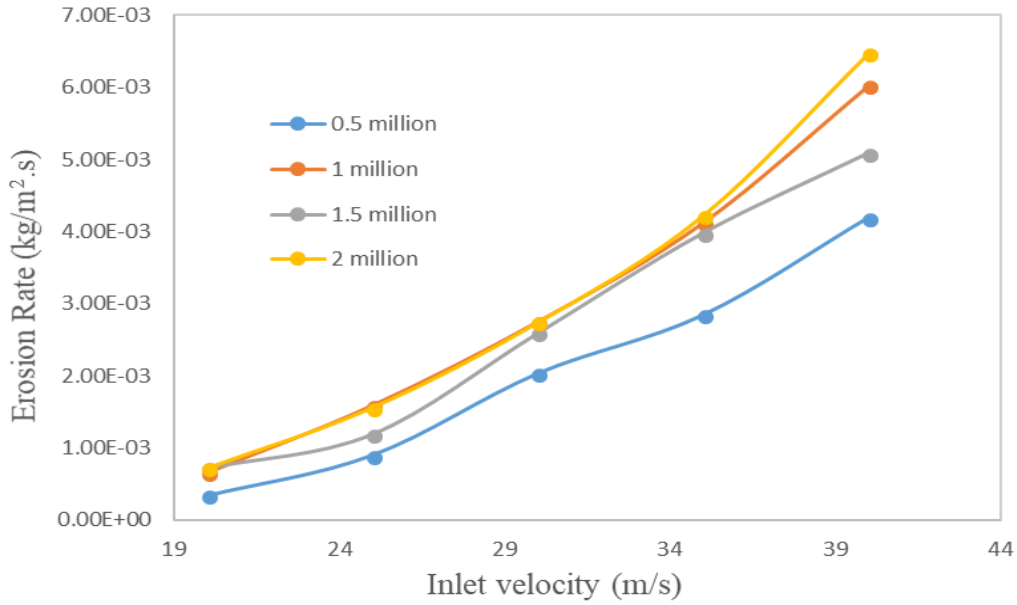
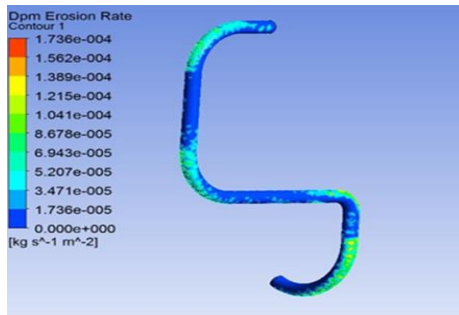


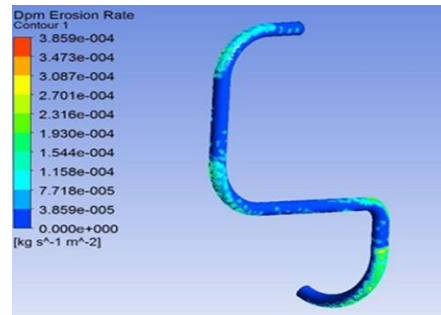
Fig. 3.6. Effect of element number on erosion rate.

3.5. Results and discussion

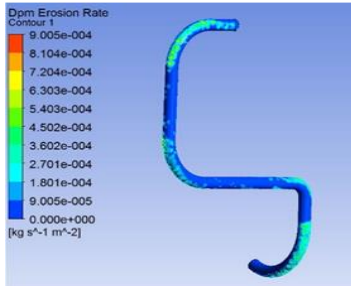
Velocity and particle size are the two main reasons for increases in erosion rate, such that when velocity increases, erosion also increases. Figure 3.7 shows the distribution of erosion rates on a bend at different inlet flow rates for solid particles of 200 (μm) and a pipe diameter of 4.52 (cm), while Figure 3.8 shows the distribution of erosion rates for solid particles of 100 (μm) and a pipe diameter of 4.52 (cm). Similarly, Figure 3.9 depicts the distribution of erosion rates on a bend at different inlet flow rates for solid particles of 70 (μm) and a pipe diameter of 4.52 (cm), and Figure 3.10 shows the distribution for solid particles of 10 (μm) and a pipe diameter of 4.52 (cm).



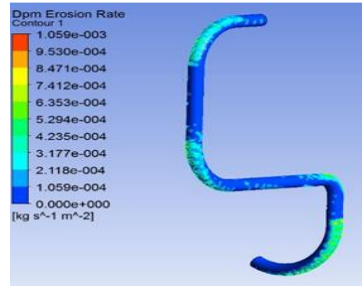
Velocity 20 (m/s)



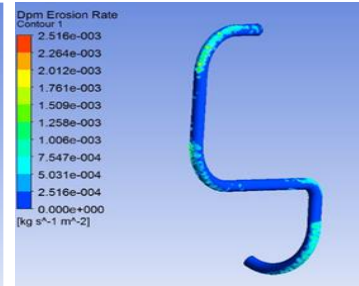
Velocity 25 (m/s)



Velocity 30 (m/s)

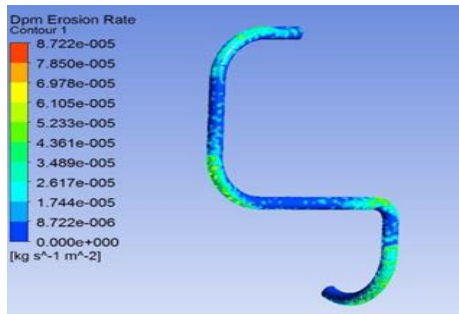


Velocity 35 (m/s)

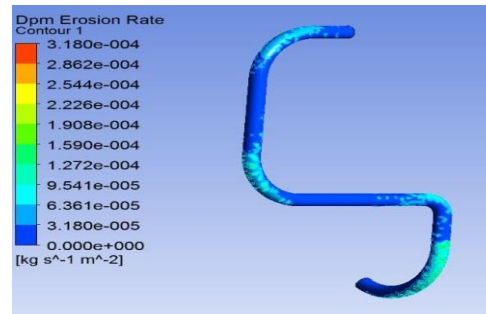


Velocity 40 (m/s)

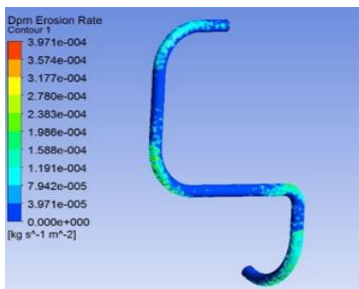
Fig. 3.7. Distribution of erosion rates for bends at different inlet flow rates at 200 (μm).



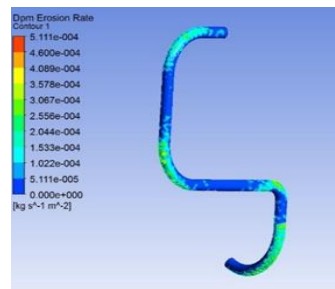
Velocity 20 (m/s)



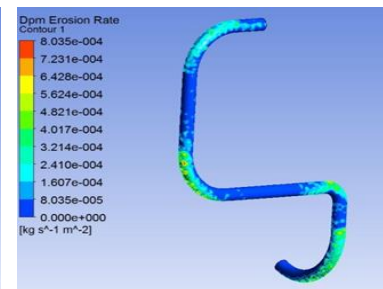
Velocity 25 (m/s)



Velocity 30 (m/s)

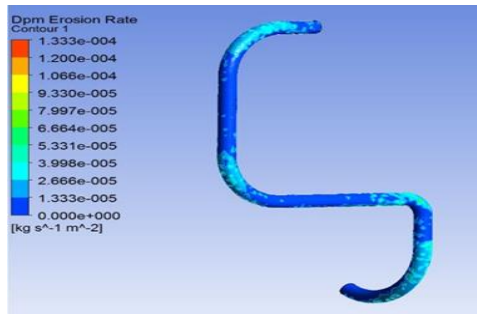


Velocity 35 (m/s)

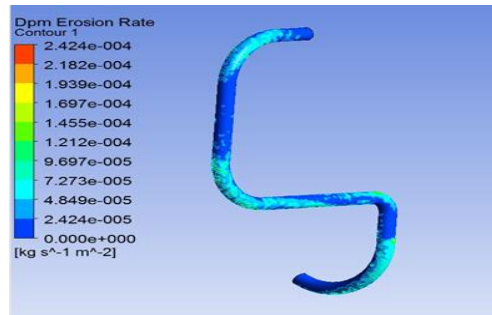


Velocity 40 (m/s)

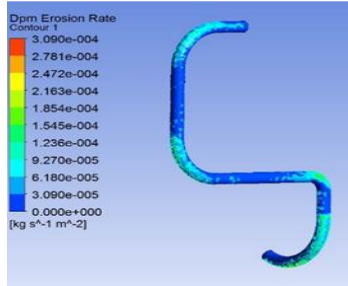
Fig. 3.8. Erosion rate for bends at different inlet flow rates at 100 (μm) and different velocities.



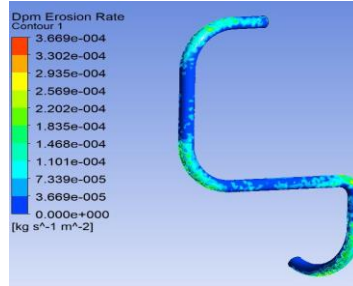
Velocity 20 (m/s)



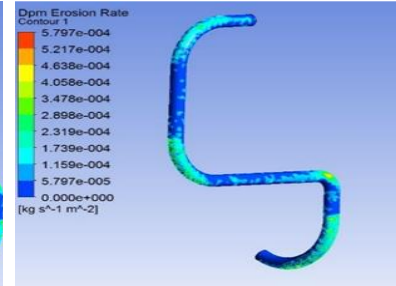
Velocity 25 (m/s)



Velocity 30 (m/s)

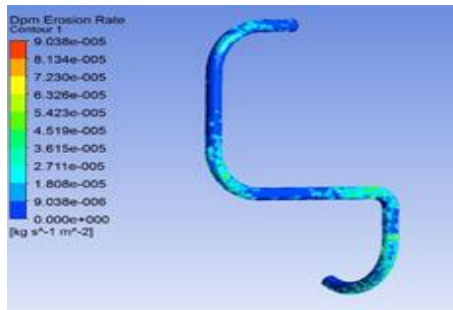


Velocity 35 (m/s)

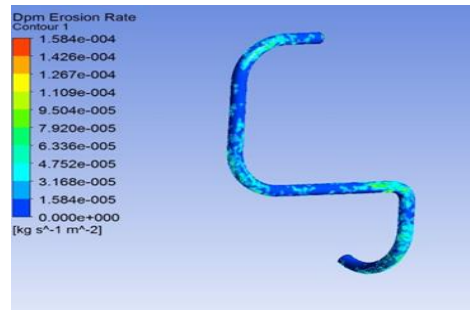


Velocity 40 (m/s)

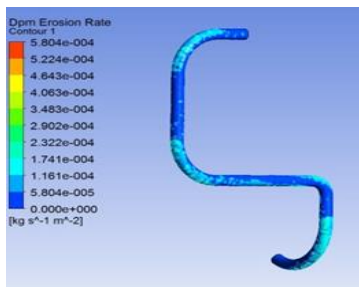
Fig. 1. Erosion rate for bends at different inlet flow rates at 70 (μm).



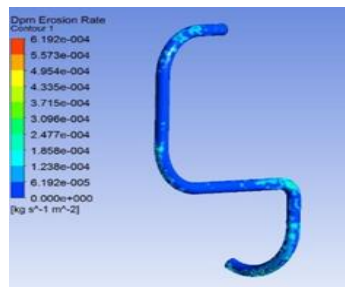
Velocity 20 (m/s)



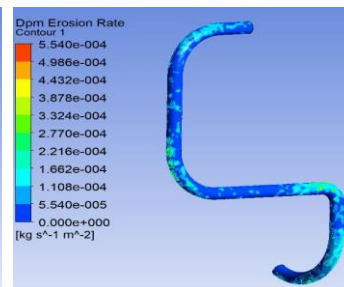
Velocity 25 (m/s)



Velocity 30 (m/s)



Velocity 35 (m/s)



Velocity 40 (m/s)

Fig. 3.10. Erosion rates for bends at different inlet flow rates at 10 (μm).

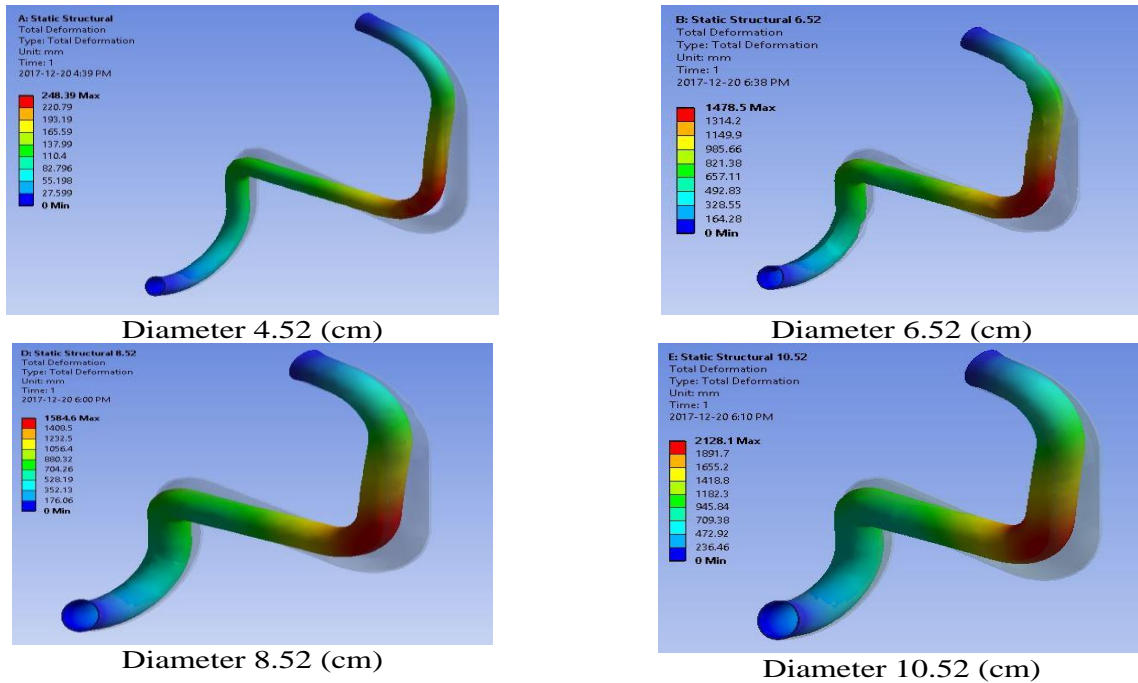


Fig. 3.11. Deformation for three different diameters of pipes at a velocity of 40 (m/s).

Diameter has a major influence on deformation. Figure 3.11 shows the deformation in four different pipes when velocity is constant in all the pipes, and when there is the same particle solid size and two fixed supports at the inlet and outlet. It is clear that deformation increases when diameter increases.

Based on Figures 3.12 and 3.13, one can generalize that the correlation between erosion rate and solid particles is proportional starting at particle sizes of $70 \mu\text{m}$ and larger. For particles smaller than $70 \mu\text{m}$, the erosion rate slightly decreases (velocity 35 m/s). In general, when velocity increases, erosion increases as well. Figure 3.12 shows the effect of both solid practical diameter and velocity on erosion rate, with the Y-axis indicating the erosion rate and the X-axis indicating particle diameter.

Regarding changes in particle diameter, erosion rates are more or less the same between 10 and $200 \mu\text{m}$ in different inlet velocities. Although, at first, there is a reduction in the erosion rate during increases in particle diameter, this changes for particle diameter $70 \mu\text{m}$ or greater. In larger

size particles (i.e., 70 μm or greater), erosion rates fall to the lowest possible levels, which is especially clear in velocities between 30 and 40 m/s. After that point, the erosion rate increases with particle diameter increases. For very large flow inlet velocities and particle diameters (100 and 200), the phenomenon is similar to that observed in the particle deposition behavior regarding shapes in duct flows [26].

This phenomenon is similar to an impact mechanism which occurs during the deposition, rebounding, and impaction process. At a velocity of 25 m/s, for smaller particles of 10 μm , the erosion goes to 70 μm and 100 μm , but the erosion rate decreases slightly due to the large inertia of 200 μm . At a velocity of 20 m/s, the erosion rises at 70 μm but then goes down at 100 μm before again rising at 200 μm . Smaller particles of 10 μm are affected more by the diffusion, turbulence, and vortex in the bend and may also have a higher impact angle, leading to higher erosion rates. Coarse particles of 100 to 200 μm are controlled by inertia and gravity and thus would erode more of the wall mass [27]. Details on this process are given in Figure 3.13.

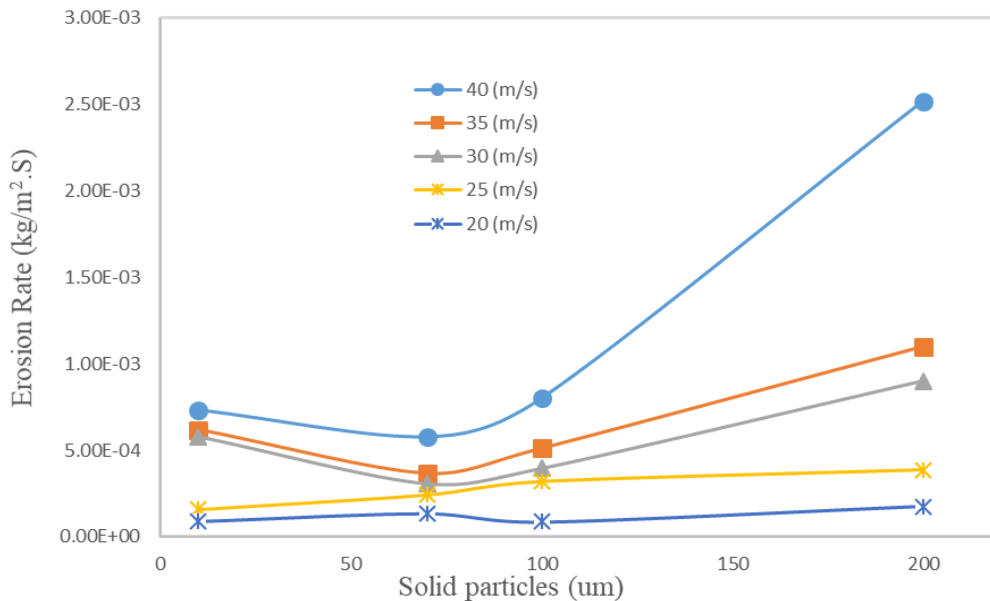


Fig. 2. Comparison of erosion rate per impact particle against the particle diameter and inlet flow velocity for larger inlet velocities of 20, 25, 30, 35 and 40 (m/s).

In Figure 3.13, the erosion rate is highly affected by particle sizes at different velocities. The maximum rate is recorded at 200 μm for all velocities, starting at 20 and going up to 40 m/s. The figure also shows that the erosion rate of 10 μm is higher than that recorded for 100 and 70 μm for velocities of 30 and 35 m/s. In general, when velocity, increases erosion increases as well.

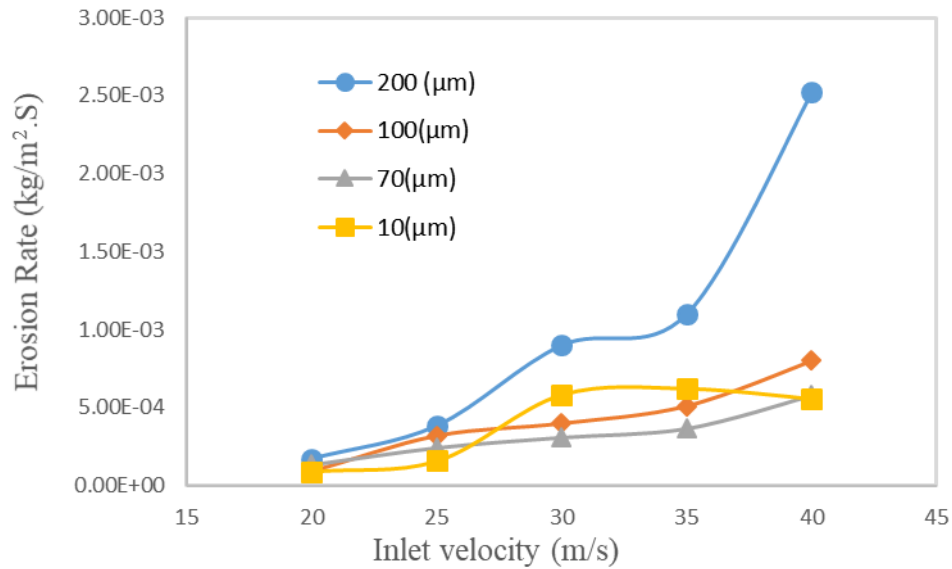


Fig.3.13. Comparison of erosion rates at different velocities and solid particle diameters 10, 70, 100 and 200 (μm).

Erosion rate is directly related to particle flow rate. Figure 3.14 shows the effect of both solid particle diameter and velocity on erosion rate, with the Y-axis indicating the erosion rate and the X-axis the flow rate for selected solid particles of 200 μm .

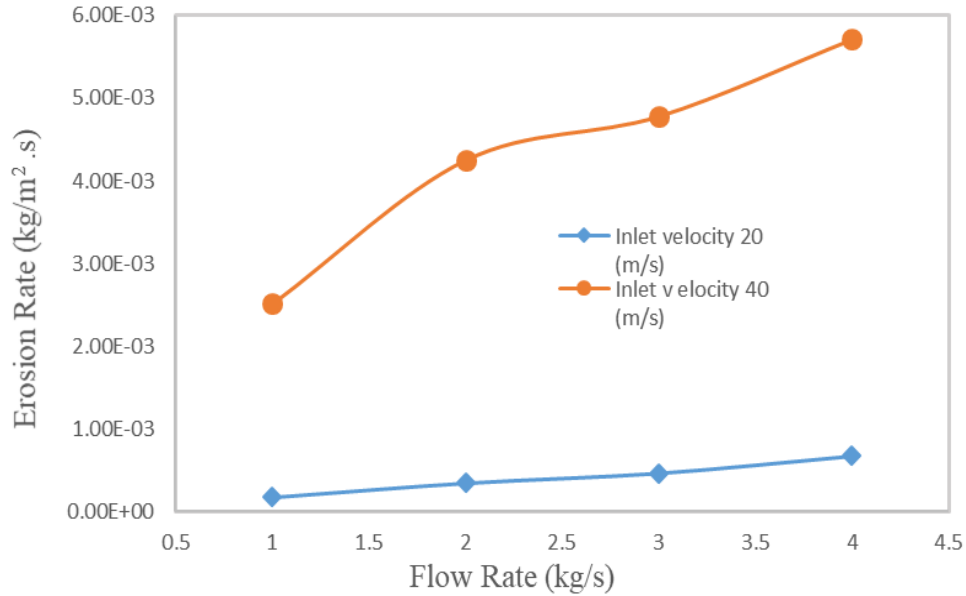


Fig. 3.14. The effect of flow rates on erosion at velocities of 20 and 40 (m/s) at the particle size 200 (μm).

The effect of solid material type on erosion rate is illustrated in Figure 3.15. As can be seen, the erosion rate caused by copper particles is slightly higher than that caused by steel particles, but is much higher than that caused by aluminum particles. The material density factor thus clearly affects the erosion rate at different velocities.

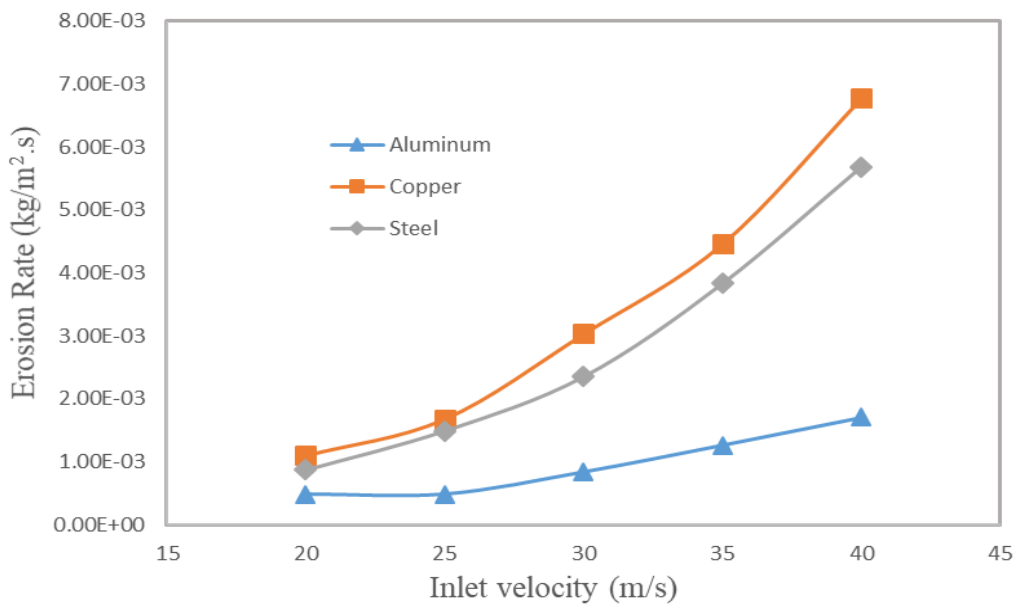


Fig. 3.15. Effect of solid particle density on erosion rates at different velocities 200 (μm).

The effect of pipe diameter on the erosion rate used is seen in Figure 17. At fixed parameters 40 m/s and 200 μm , the erosion rate reduces as the pipe diameter increases from 4.52 to 6.52 cm, at which point the correlation between erosion rate and pipe diameter is reversed. The effect of pipe diameter change is negligible between 6.52 and 10.52 cm, but then the erosion rate is nearly constant, with particle-clashing at the pipe wall reducing in tandem with increases in diameter.

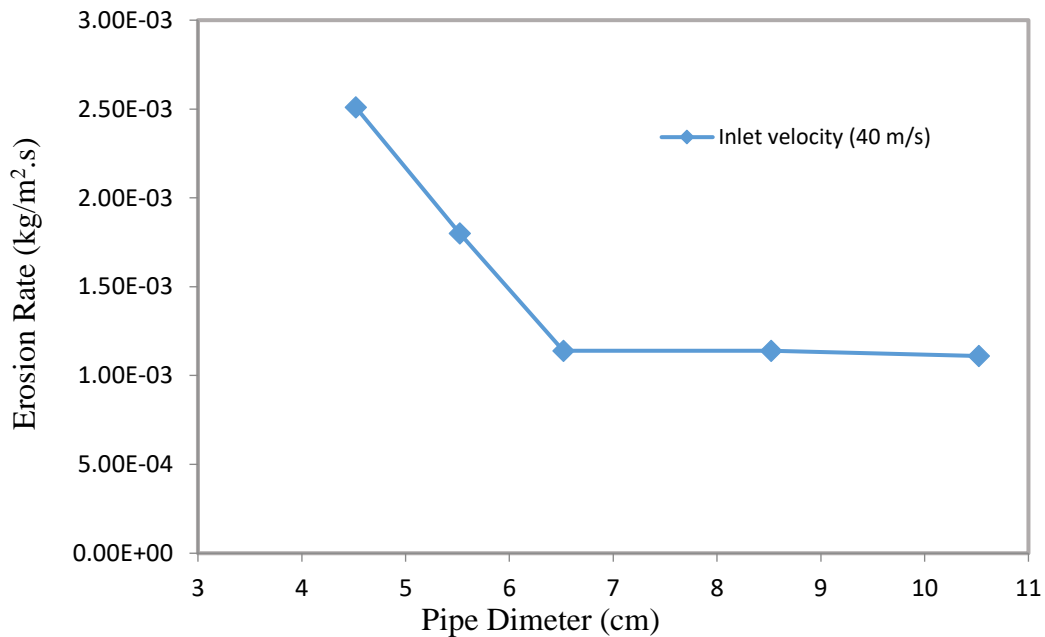


Fig. 3.16. Effect of pipe diameter on erosion rates at a velocity of 40m/s and particle size of 200 (μm).

Only a few studies have been performed to examine the effect of carrier fluid viscosity on erosion rate. The model predicts pipeline erosion at different velocities and at solid particles of 200 μm , and decreases in pipeline erosion rates as viscosity increases. The results shown in Figure 18 follow this trend up to a certain viscosity, which is multiplied five times each, starting at 0.2 mPa.s and going to 625 mPa.s. However, at higher viscosities, the erosion rate increases with increasing viscosity, as shown in Sun et al. [26] for erosion rates for 90° elbows at various carrier fluid viscosities. The researchers Sun et al. [26] found only slight increases in erosion rates when

the viscosity was increases between settings of 125 mPa.s and 625 mPa.s. They [32] attributed their findings to particle size as well as particle shape (spherical).

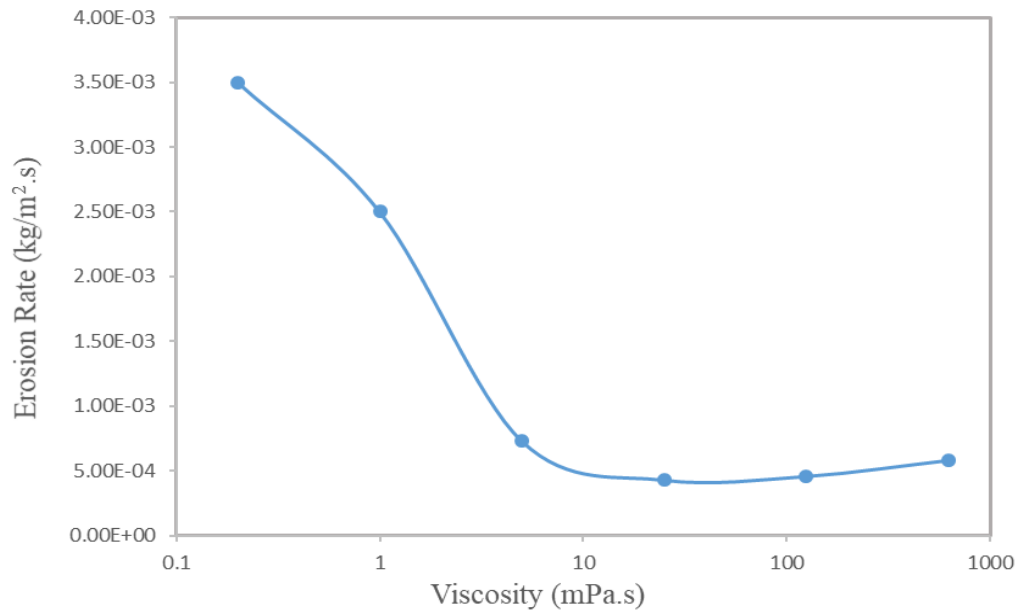


Fig.3.17. Effect of viscosity on erosion rates at a velocity of 40m/s and particle size of 200 (μm).

Chapter 4 Four-phase flow investigation of erosion in intricate pipelines with bends using CFD simulations.

Abstract: — In the oil and gas industry, issues around solid particle erosion and increasing erosion rates are ongoing challenges. Numerous factors come into play when trying to resolve these problems, such as the shape and size of the particles causing the erosion, and the ductility of the pipelines carrying them. As investigated in the literature, these flows can come into contact with affected surfaces at different velocities and angles. Numerical and experimental research indicates that in slow flows of phases in dense gas or liquid (e.g., slurry transport), particle impact angles tend to be so narrow that they are difficult to test. The present research study examines erosion rates in relation to primary and secondary phase flows. In order to simulate four-phase flows in a pipeline with an arc and two bends under the impact of solid/liquid particle-initiated erosion, the CFD (computational fluid dynamics) code ANSYS FLUENT is used. The simulations in this work measure fluid velocities and erosion rates/locations for 200-micron sand particles, applying liquid velocities measuring 20, 25, 30, 35 and 40 m/s in CFD-based tests. The results show that if ethane exerts the primary phase impacts with 200 microns of flow material, the erosion rate is $9.760 \times 10^{-3} \text{ kg/m}^2 \cdot \text{s}$ at speeds of $\sim 40 \text{ m/s}$. However, if methane comprises the carrier fluid with 200 microns of flow material, the erosion rate is $1.006 \times 10^{-2} \text{ kg/m}^2 \cdot \text{s}$ at sine speeds of $\sim 40 \text{ m/s}$. The present study also models how the flow particles affect the carrier fluid (e.g., methane, water, ethane), applying both one-way and full coupling. In addition, the turbulence effect exerted in a medium by the particle dispersion force against particles is examined in detail. Finally, the primary and secondary phases' impact parameters are determined in relation to frequency and speed of impact on outer wall bends. Any interactional force occurring between the particles and the carrier fluid has been considered as a measure of VOF (volume of fluid) momentum transfer.

Keywords: Primary phase, Erosion, Velocity, Solid Partible, CFD.

4.1. Introduction

Several different kinds of commercial drilling processes in the oil and gas industry must take into account particulate multiphase flow (a mixture of oil, gas, water, and sand), which is characterized as a constant and continuous carrier phase that effectively disperses the solid phase. Damage due to erosion can be initiated by sand particles blasting through pipes under high pressure. These types of erosive particulate flows also occur in other major industries, such as aero-space and energy production infrastructures [33].

When gas and particle fluid mixtures near a bend in a pipe, the fluid phase flow structure diverges into a double vortex, resulting in extreme particulate phase separation caused by centrifugal forces acting on the flow. The interactions which occur between the fluid and the particles (including particle-particle and particle-wall collisions and rotational or gradient forces) for the most part determine not only pressure drop and fluid velocity distribution but also particle behavior. Extensive research has been carried out recently on the experimental, numerical and pneumatic conveyance of particle and fluid flows. In the researchers simulated particle collisions on coarse pipe surfaces and looked at the non-sphericity of particles using numerical simulations and tests. The researcher investigated a particle-particle collision model and proposed a particle-wall collision model that takes into consideration how the shadow effect might inhibit rebounding.

In other studies, the numerical and physical modelling for erosion which can occur in elbows, tees, pipe bends, etc., was examined. Computational fluid dynamics (CFD) is currently the favoured approach for predicting erosion caused by solid particles in ducts and curved pipes and has been for the past few decades. Using CFD, several different empirical, semi-empirical and analytical approaches were modeled. In Meng and Ludema [34] presented an overview of the main

erosion models, highlighting 28 which pertained to particle-wall erosion. While investigating these 28 models, the researchers discovered 33 parameters which were applied in the models, although each model usually applied no more than five in total [34]. The broad range of parameters in general dealt with how much material was being sloughed off a specific surface due to erosive action. The researchers' findings revealed that erosion prediction is a fluid concept that cannot be universally framed. Meanwhile, in the researcher suggested applying an analytical method to predict wear and tear occurring in bendable materials [35].

It is typical for oil and gas sites to share pipelines with other sites to move their product from wells to the next transport or refinery site. Hence, in these shared pipelines, even if only one of several wells is transporting a multiphase fluid, the entire pipeline is considered multiphase. Ratios differ among oil and gas mixtures, but the majority comprise crude oil and some dissolved gas. In fact, natural gas makes up most of the flow present in oil and gas separator venting pipes, along with a smaller fraction of heavy hydrocarbon condensate and water. So, for instance, gas flowing from a coalbed methane gas site well would also include water condensation, turning the flow into multiphase. This is a typical transportation mode from well sites, as to install more than one pipe would not be economical. There are also cases where the installation of gas/liquid separators would not be feasible (e.g., ecologically sensitive areas and urban zones).

Indeed, the surrounding geography of well sites has a significant impact on the type of pipeline that is best used. For example, single-phase pipelines function well in hilly or mountainous regions because any pressure lost at the ascent would be recouped at the descent. However, two-phase flows would not be suitable, as any pressure lost going uphill would not be recouped in the descent due to the lesser density of the material flow. Hydraulics and choosing optimal routes play a major role in resolving these kinds of flow equalization issues.

In two-phase pipelines, gas/liquid distribution can differ from pipe to pipe and flow to flow. Such differences can affect the factors of heat/mass transfer and mechanical interrelationships inherent in two-phase flows, making the process extremely complex. The calculation models presently being used to describe multiphase flow vary in their degree of usefulness, but such a discussion on the merits of each model does not fall within the scope of our paper. Instead, the present study looks at the gas and liquid two-phase Beggs-Brill approach that combines a route-optimization algorithm with hydraulic simulation. Additionally, this study will examine how primary and secondary phases impact erosion rates. Both CFD code and ANSYS FLUENT will be used in the four-phase flow simulation for a pipeline that is experiencing a high erosion rate caused by both solid and liquid particles in the flow. The erosion rate will be determined by the amount of pipeline wall lost and will be calculated by applying the Finnie model for bendable materials [36].

4.2. Geometry and meshing

The ANSYS Fluent Directed Mesh Inflation approach has been applied to formulate the material for the simulation of horizontal pipeline two-phase flow. Compared to other meshing approaches, the main benefits of employing Directed Mesh Inflation in this simulation is its relatively short computational time, small cell number, and parametric grid-building capability for use in multi-block formats. Simulation users are able to determine the exact number of inlet cross-section divisions when applying the path mesh, thus allowing for the construction of quadrilateral surfaces. Additionally, users are able to determine the number of pipeline layers through the application of volume distribution, as shown in Fig. 4.1.

Figures 4.1 and 4.2 illustrate how hexahedral grid cells have been applied to develop volume mesh by extruding quadrilateral surfaces for every layer throughout the pipeline length. Further

mesh grid details for the grid being developed in the present study are given in Table 4.1 As can be seen, this type of grid forms a fine cross-sectional mesh without the need for a longitudinal one of equivalent length.

When probes occurring in fluid domains are changed to walls from freestream flows, there is a non-linear decrease in the speed of the flow to the zero velocity point of wall encounter. Zero velocity, when framed in CFD, is termed as a ‘no-slip’ phase. The extreme shifts in speed that occur in fluids as they approach a wall must be included in the velocity calculations for the CFD simulations referring to the gradient condition. In this formulation, we can apply inflation layer meshing to determine the appropriate boundary layer regions for wall-bounded flows, which are typically turbulent and complex. The flow behaviors must, however, be determined in order to formulate valid CFD data for pipeline engineering related to potential problem areas such as separation points and pressure drops [24].

Flow fields, turbulence models and inflation mesh feature significant interdependence factors. Therefore, in order to better understand each element of boundary layers, either the total profiles of each layer needs to be resolve or empirical wall functions need to be done by decreasing cell counts. Figure 4.1 example charts maximum layer counts for the ANSYS approach [24].

Table 4.1 DETAILS OF MESH

Nr. of elements	99751
Nr. of nodes	39012
Element size [mm]	0.617
Maximum layers	5

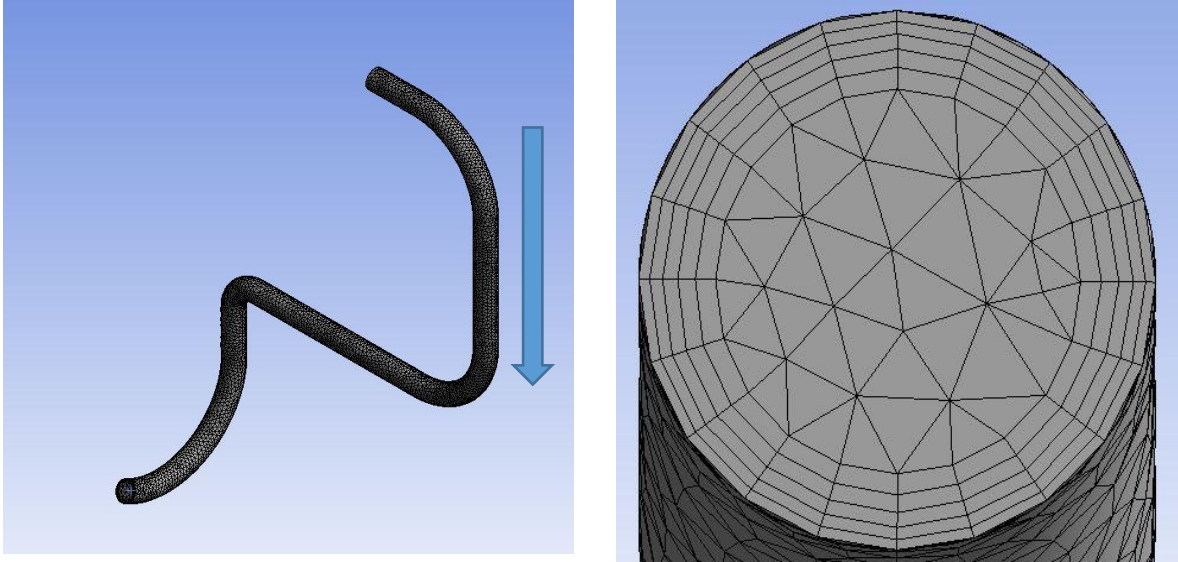


Fig. 4.1 Geometry and mesh in ANSYS

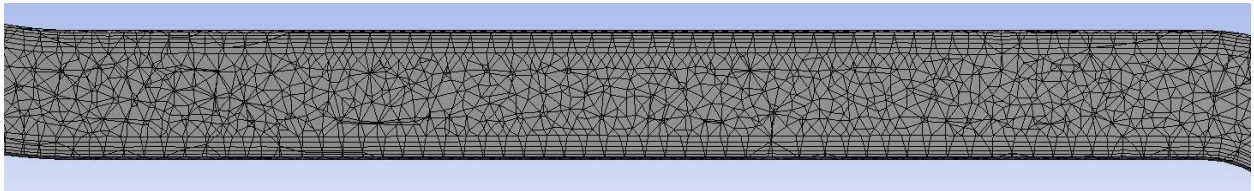


Fig. 4.2 Cut in the pipeline showing detail of mesh

4.3. Discrete phase model

In FLUENT, there is also a specific model for simulating the transport of particles through continuous flow fields. In this discrete phase model (DPM), a motion equation uses a Lagrangian coordinates frame to represent the discrete phase occurring in a continuous phase, giving a reasonable calculation of possible particle trajectory. The local continuous phase conditions are applied to solve the particle force balance equation, as follows:

$$\frac{dv_p}{dt} = F_D(v_f - v_p) + g \frac{(p_p - p_f)}{p_p} + F_x \quad (4.1)$$

where v_p and v_f are the particle and fluid velocities, ρ_p and ρ_f are the particle and fluid densities, respectively, g is the gravitational acceleration, F_x is a term accounting for additional forces, $F_D (v_f - v_p)$ is the drag force per unit particle mass, F_D is dimensionally an inverse of time and reads:

$$F_D = \left(\frac{1}{\tau_a} \right) a = \left(\frac{18\mu}{\rho_p D_p^2} \right) \left(\frac{C_D \text{Re}}{24} \right) \quad (4.2)$$

where τ_a is the aerodynamic response time for the particle, Re is the Reynolds number for the particle referred to the relative velocity and C_D is the drag coefficient

$$\text{Re} = \frac{\rho_f |v_f - v_p| D_p}{\mu_f} \quad (4.3)$$

$$C_D = a_1 + \frac{a_2}{\text{Re}} + \frac{a_3}{\text{Re}^2} \quad (4.4)$$

with coefficients a derived in [13] for two-phase flows. In order to confer position and speed to the particle and as a way of closing the solving equation set, Eq. (4.1) and the Lagrangian frame trajectory equation, $ds/dt = v_p$, are combined, showing s as the abscissa of trajectory [37].

It should be noted that the impact of turbulence on particle dispersion in turbulent flows is far from negligible and must be considered in the calculations. In the so-called Eddy lifetime discrete random walk (DRW) stochastic model, turbulent dispersion is estimated by combining the trajectory equations of each particle and applying instantaneous fluid speed (or velocity) throughout the course of the particle pathway. Hence, fluid velocity for particle location is formulated as $v = \tilde{v} + v'$, where \tilde{v} indicates mean fluid phase velocity and v' the turbulent portion in fluid velocity. Gaussian distributed random fluctuation is used to formulate turbulent

contribution, granting it a constant status in relation to the solution advancement time step Δt which covers DRW τ_e , as given below [37].

$$\tau_e = 0.30 \frac{k}{\varepsilon} \quad (4.5)$$

4.3.1. Volume Fraction Equation

In the present study, a ternary fluid flow comprising two liquids and one gas in immiscible phases is investigated. Specialised models are used to ensure the code can deal appropriately with the various multiphase flow types it will encounter. Despite its widespread use, existing CFD is still unable to simulate multiphase flows in fine detail because of the complicated structure in the flows (e.g., interphase heat transfer, phase transition, etc.). Another huge challenge is dealing with the assumed homogeneity of phases which is inherent in the CFD program. Nevertheless, we proceed with this in mind and consider the flow mixture as being homogenous through the mesh material.

Next, we choose the VOF (volume of fluid) to model the fluid phase simulations and deactivate the simulation aspect pertaining to the interface position between fluids as per the homogenisation referenced in the previous section. After solving applicable momentum balance equations of the mixture into a single set, we evaluate the phase volume fractions of each phase for all individual computational cells within the domain, considering the gas and liquid phases incompressible. Finally, we solve a continuity equation to find the volume fraction of the phases in order to track the interfaces between phases. The equation for the q^{th} phase is expressed as follows:

$$\frac{1}{p_q} \left[\frac{\partial}{\partial t} (a_q p_q) + \nabla \cdot (a_q p_q \vec{V}_q) = S_{aq} + \sum_{p=1}^n (m_{pq} - m_{qp}) \right] \quad (4.6)$$

where m_{qp} denotes mass transfer out of phase q and towards phase p , and m_{pq} indicates mass transfer out of phase p and towards phase q . For our purposes here, the source term to the right of Eq. (4.6), S_{a_q} implies zero; however, either a constant or a user-defined mass source of every phase can be applied instead. Note that because the volume fraction equation is not solved in the primary phase (but is rather done later via explicit or implicit time calculations), we can formulate the primary-phase volume fraction as shown in Eq. 4.7 below:

$$\sum_{q=1}^n a_q = 1 \quad (4.7)$$

4.3.2. Implicit Formulation

To use implicit formulation expression, we must first discretize the volume fraction equation as follows:

$$\frac{a_q^{n+1} p_q^{n+1} - a_q^n p_q^n}{\nabla t} V + \sum_f (p_q^{n+1} U_f^{n+1} a_{a,f}^{n+1}) = \left[Saq + \sum_{p=1}^n m_{pq} - m_{qp} \right] V \quad (4.8)$$

$n+1 =$ index for current time step

$n =$ index for previous time step

$a_q^{n+1} =$ cell value of volume fraction at time step $n+1$

$a_q^n =$ cell value of volume fraction at time step n

$a_{q,f}^{n+1} =$ face value of the q^{th} volume fraction at time step $n+1$

$U_f^{n+1} =$ volume flux through the face at time step $n+1$

$V =$ cell volume

Furthermore, because the current time step's volume fraction also represents a function related to the current time step's other quantities, we must solve a scalar transport equation iteratively in every secondary-phase volume fraction and for every time step. To do this, a spatial discretization

scheme must be applied for interpolating face fluxes, choosing from ANSYS Fluent schemes. These are presented in detail in the Users' Guide, under the section *Spatial Discretization Schemes for Volume Fraction*. Implicit formulation is applicable in both steady-state and time-dependent formulation, as presented in the guide's *Choosing Volume Fraction Formulation* sub-section [31].

4.3.3. Explicit Formulation

The explicit formulation is time-dependent, and the volume fraction is discretized in the following manner:

$$\frac{a_q^{n+1} p_q^{n+1} - a_q^n p_q^n}{\nabla t} V + \sum_f (p_q^{n+1} U_f^{n+1} a_{a,f}^n) = \left[S_{aq} + \sum_{p=1}^n (m_{pq} - m_{qp}) + S_{aq} \right] V \quad (4.9)$$

$n + 1$ = index for new (current) time step

n = index for the previous time step

$a_{a,f}$ = face value of the q^{th} volume fraction

V = volume of cell

U_f = volume flux through the face, based on normal velocity

Because volume fraction for current time steps must be formulated according to quantities from previous time steps, there is no requirement for explicit calculations to have an iterative solution for the transport equation at every time step, in which case face fluxes are interpolated by applying CICSAM, Geo-Reconstruct, or Compressive and Modified HRIC as capturing schemes. Relevant schemes on explicit formulation in ANSYS Fluent can be found in the subsection *Spatial Discretization Schemes for Volume Fraction* in the Users' Guide. It is worth noting here that ANSYS Fluent refines time steps automatically in relation to volume fraction equation integration, and that these calculations can be adjusted using the Courant number. Specifically, volume fractions can be revised at every time step or singularly at every iteration for every time step (see

the Users' Guide sub-section *Setting Time-Dependent Parameters for the Explicit Volume Fraction*) [31].

4.3.4. Erosion Rate

Next, the model for calculating erosion estimation is chosen based on an experimentally-sourced formulation:

$$R_{\text{erosion}} = \sum_{p=1}^{N_{\text{particles}}} \frac{\dot{m}_p C(d_p) f(\alpha) v^{b(v)}}{A_{\text{face}}} \quad (3.3)$$

where $C(d_p)$ is a function of particle, α is the impact angle of the particle path with the wall face, $f(\alpha)$ is a function of impact angle, v is relative particle velocity, $b(v)$ is a function of relative particle velocity, and, A_{face} is the area of the cell face at the wall.

Default values are: $C = 1.8 \times 10^{-9}$, $F = 1$ and $b = 0$ in ANSYS Fluent. We can modify formulations expressing erosion models such that they take the format of a general equation for erosion rate, as expressed in Equation 3.3 So, for instance, we can rewrite the Tulsa Angle Dependent Model [25].

$$ER = 1559B^{-0.59}F_s v^{1.73} f(\alpha) \quad (3.4)$$

as Equation (3.4) by making substitutions as follows:

$$\begin{aligned} v^{1.73} &= v^{b(v)} \\ 1559B^{-0.59}F &= C(d_p) \end{aligned}$$

Where ER indicates erosion rate, B denotes Brinell hardness, and F represents the particle shape coefficient.

4.4. Boundary conditions:

Table 4.1 BAROMETERS AND INFORMATION FOR THE SIMULATION

Fluent Setting	
Inlet	30, 35 & 40 (m/s)
Outlet	Pressure outlet
Wall	No Slip
Multiphase	Volume of Fluid
Turbulent	k-epsilon
DPM	ON
Injection Surface	
Velocity	30, 35 & 40 (m/s)
Diameter	100 (μm)
Density	1500 (kg/m ³)
Total Flow Rate	1 (kg/s)
Discrete Phase	
Velocity	30, 35 & 40 (m/s)
Density	0.6679, 1.263 & 998.2 (kg/m ³)
Pipe Information	
Length	177 (cm)
Diameter	4.52 (cm)
Material	Aluminum

4.5. Results and discussion

The outcome of our research points to primary phase flow as being the key driver in increases of erosion rates. Figure 4.3 shows erosion rate distribution occurring near a bend for different rates of inlet flow. As can be seen, the primary phase water and solid particles are $200\ \mu\text{m}$, and the diameter of the pipe is $4.52\ \text{cm}$. Figure 4.4 illustrates erosion rate distribution for primary phase Methane at $200\ \mu\text{m}$ and a pipe with a diameter of $4.52\ \text{cm}$. In Fig. 4.5, we can see erosion rate distribution occurring near a bend for different rates of inlet flow. In this figure, the primary phase Ethane at $200\ \mu\text{m}$ and the pipe has a diameter of $4.52\ \text{cm}$. If water forms the primary phase, Methane and Ethane have a volume fraction of 0.02 and 0.05 , respectively, but if Methane forms the primary phase, Methane and water have a volume fraction of 0.05 and 0.02 , respectively.

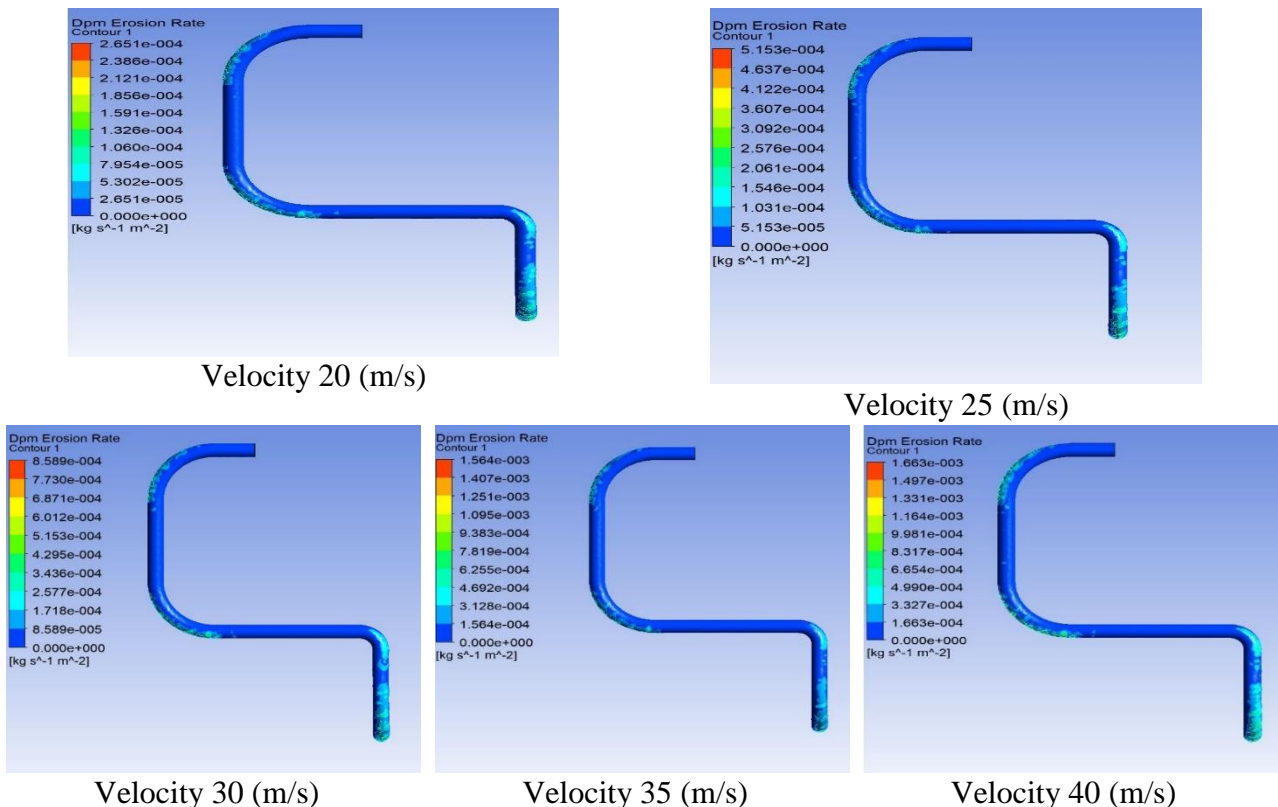
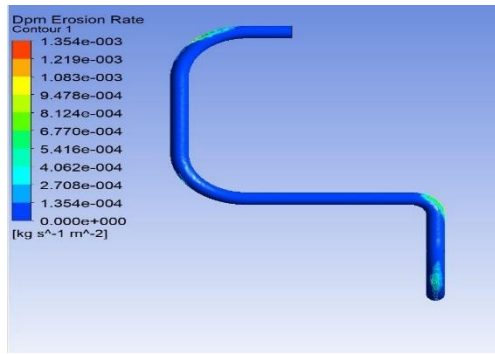
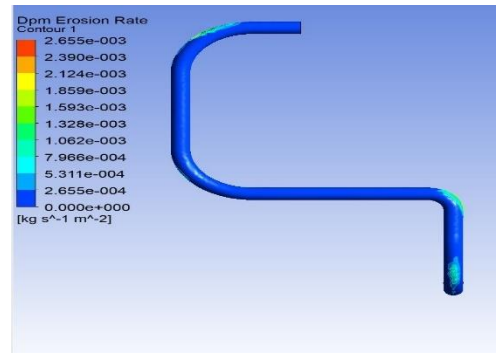


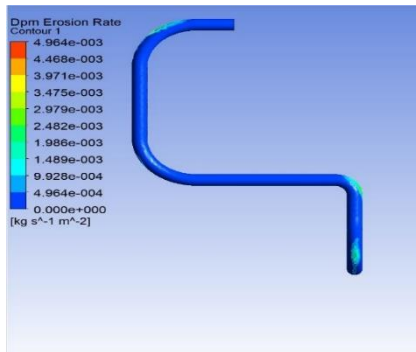
Fig. 4.3. Distribution of erosion rates for bends when the primary phase is water at different inlet flow rates at $200\ (\mu\text{m})$.



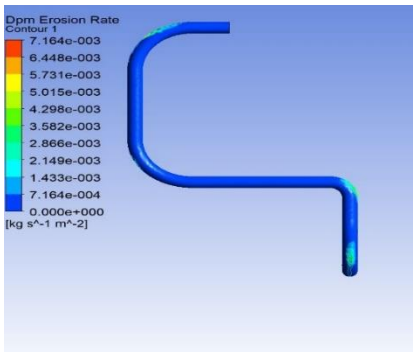
Velocity 20 (m/s)



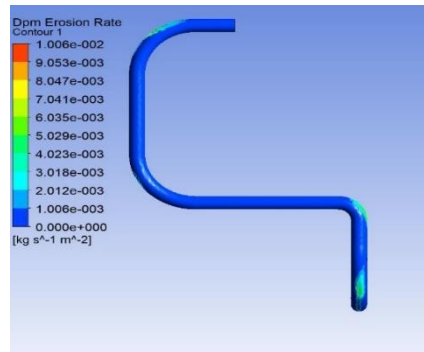
Velocity 25 (m/s)



Velocity 30 (m/s)

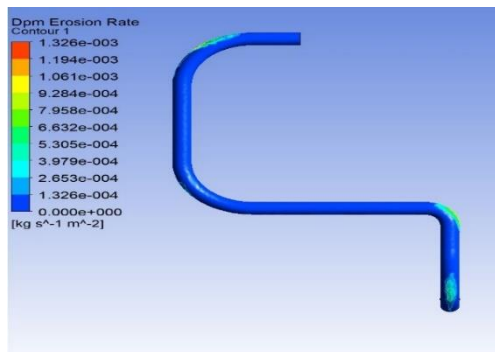


Velocity 35 (m/s)

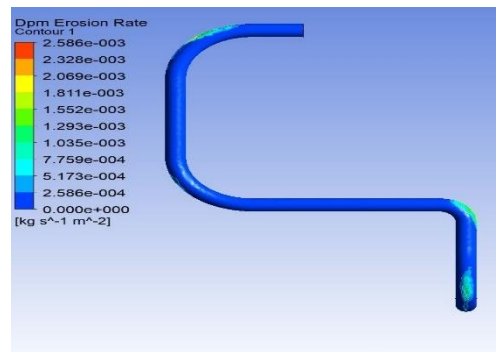


Velocity 40 (m/s)

Fig. 4.4. Distribution of erosion rates for bends when the primary phase is Methane at different inlet flow rates at 200 (μm).



Velocity 20 (m/s)



Velocity 25 (m/s)

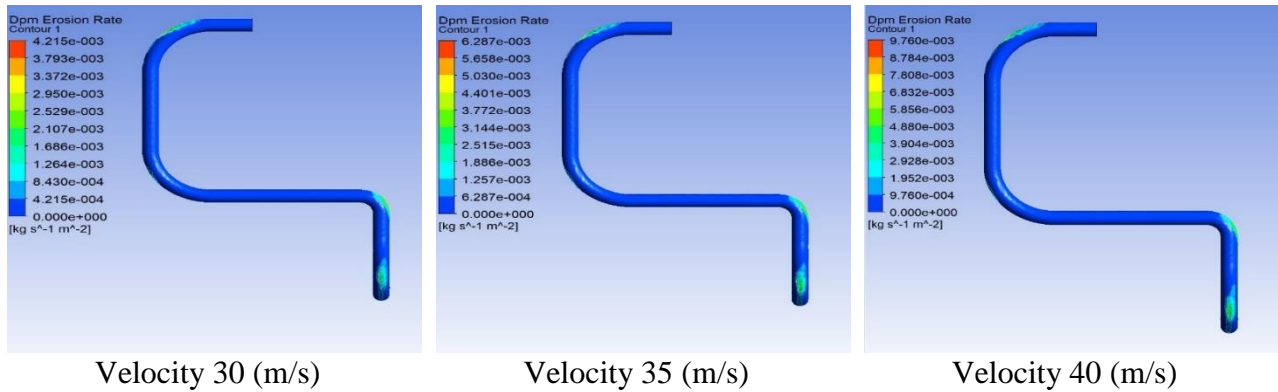


Fig. 4.5. Distribution of erosion rates for bends when the primary phase is Ethane at different inlet flow rates at 200 (μm).

As mentioned previously, the main cause of increases in erosion rates appears to be primary phase flow. Furthermore, if the primary phase is a gas, the erosion rate is higher than when the primary phase is a liquid. The graph in Fig. 4.6 shows erosion rate distribution near a bend for a number of different rates of inlet flow. As can be seen, the measurements for primary phase as water, Ethane and Methane are 40 m/s, while the diameter of the pipe is 4.52 cm. If water forms the primary phase, the Methane and Ethane volume fraction is 0.02 and 0.05, respectively, but if Methane forms the primary phase, the Methane and water fraction is 0.02 and 0.05, respectively.

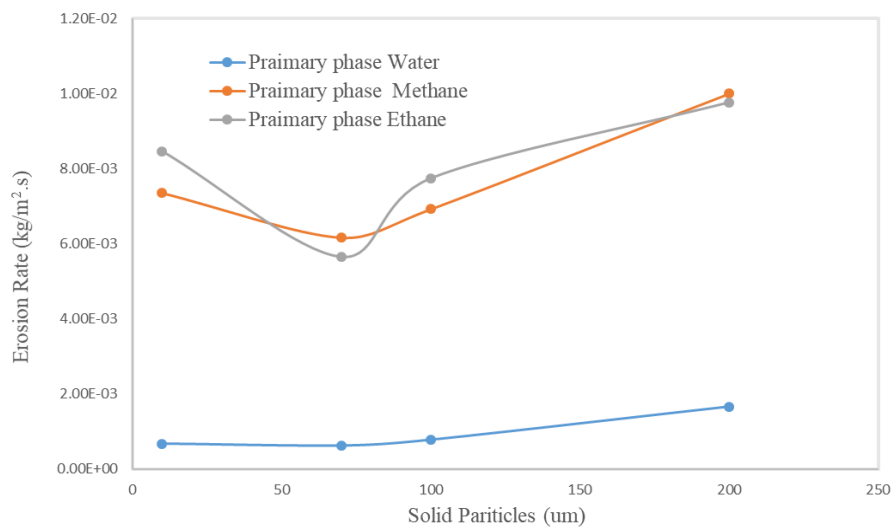


Fig. 4.7. Comparison of erosion rates for different solid particles and primary phase flow rates.

For particle diameter changes, erosion rates remain relatively similar from 10 and 200 μm for various inlet speeds. As shown earlier in Fig. 13, this effect is comparable to impact mechanisms that can happen in the processes of impaction, rebounding and deposition. At speeds of around 25 m/s, particles measuring approximately 10 μm result in erosion rates of $\sim 70\text{-}100 \mu\text{m}$. These rates of erosion begin to decrease, however, at inertia approaching 200 μm . For speeds of around 20 m/s, the erosion rate increases near 70 μm , followed by a decline near 100 μm , followed by a second increase near 200 μm . Interestingly, tiny particles (smaller than 10 μm) have higher rates of erosion (likely caused by higher impact angles) and are more influenced by turbulence and diffusion. On the other hand, larger particles (e.g., 100-200 μm), being more affected by gravity and inertia, cause greater erosion of walls [27]. Figures 25 to 27 provide details on these mechanisms.

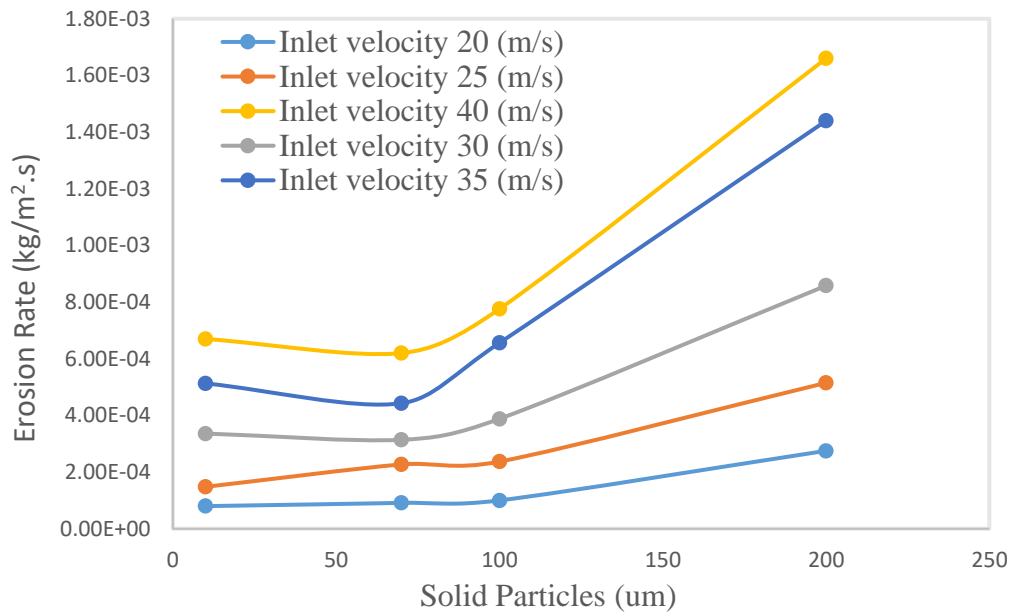


Fig. 4.8. Comparison of erosion rate per impact particle against particle diameter and inlet flow velocity for larger inlet velocities of 20, 25, 30, 35 and 40 m/s, with water as a primary phase.

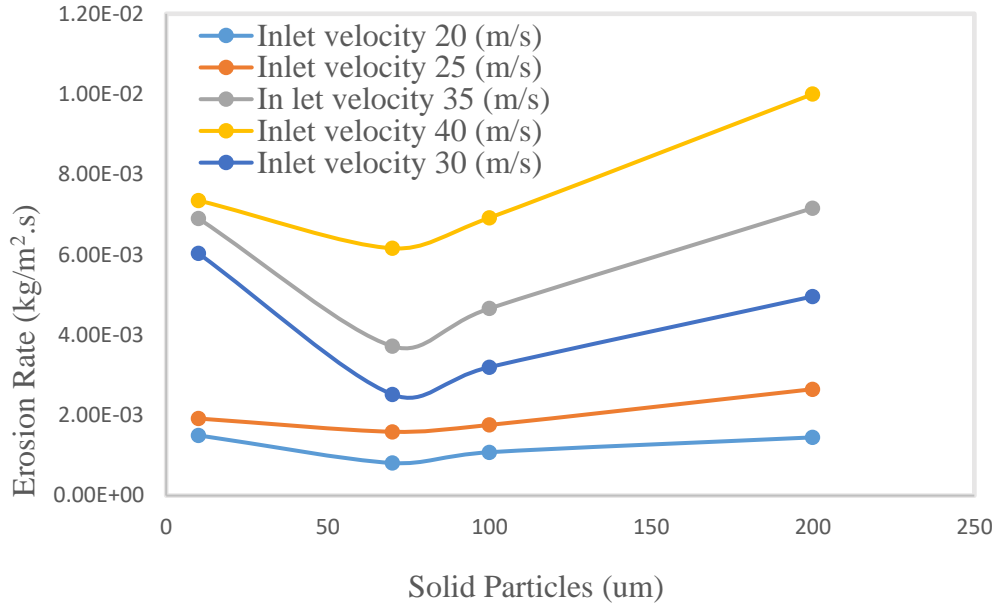


Fig. 4.9. Comparison of erosion rate per impact particle against particle diameter and inlet flow velocity for larger inlet velocities of 20, 25, 30, 35 and 40 m/s, with Methane as a primary phase.

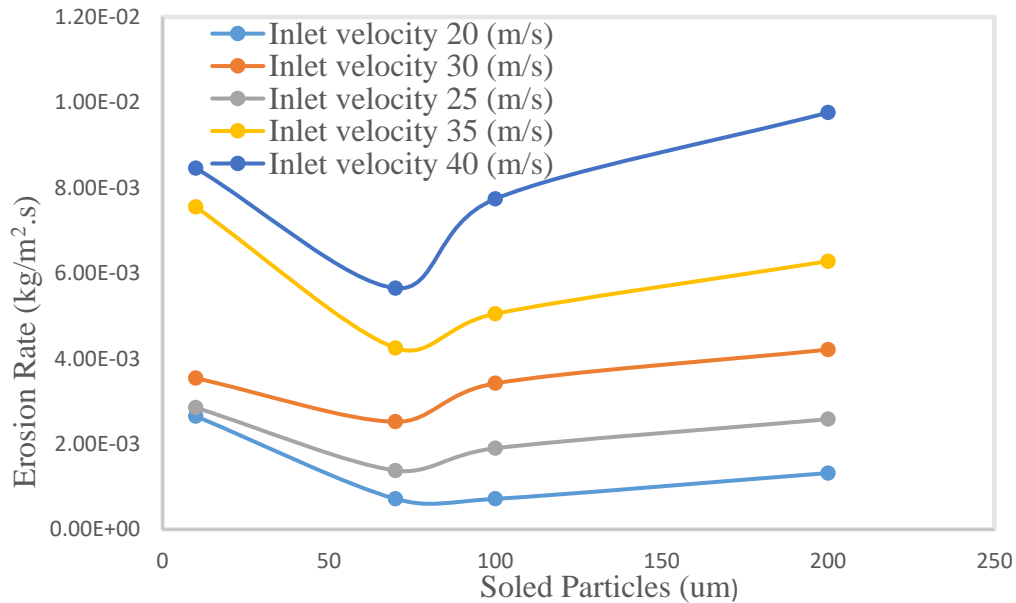


Fig. 27. Comparison of erosion rate per impact particle against particle diameter and inlet flow velocity for larger inlet velocities of 20, 25, 30, 35 and 40 m/s, with Ethane as a primary phase.

Figure 4.10 shows particle size under various speeds influencing erosion rates at ethane forms a primary phase. For every speed, beginning with 20 m/s and increasing to 40 m/s, maximum rates are 200 μm for all velocities. From the same figure, we can also see that, at speeds of 20-40

m/s, erosion rates of around 10 μm are greater compared to those at around 70-100 μm . From this, we can conclude that faster speeds lead to greater erosion.

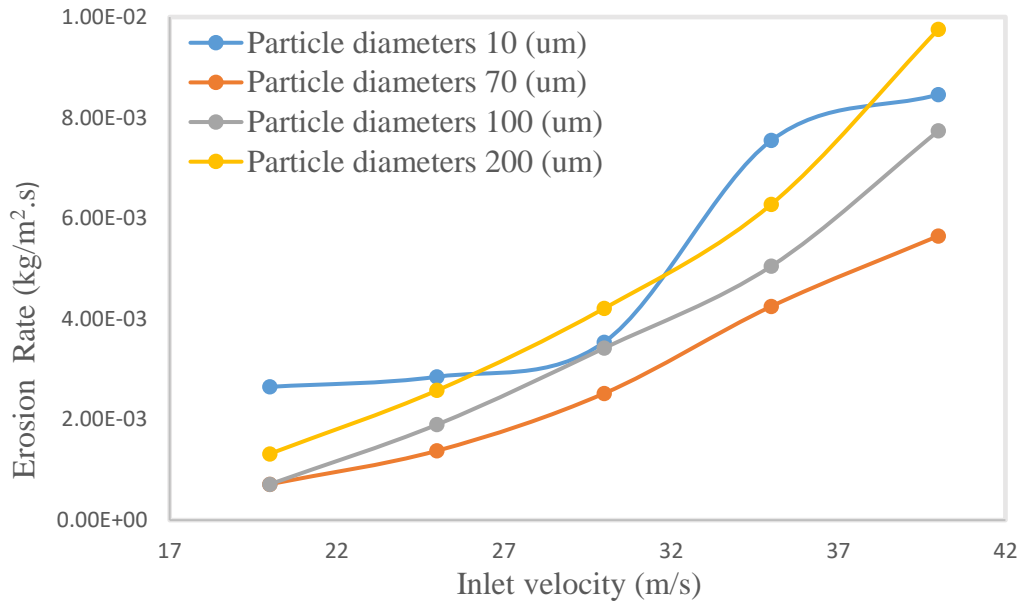


Fig. 4.10. Comparison of erosion rates at different velocities and solid particle diameters of 10, 70, 100 and 200 (μm).

Figure 4.11 depicts how pipe diameter affects erosion rates with ethane as a primary phase. As can be seen, for parameters of 40 m/s and 200 μm , there is a decrease in erosion rate with expansion of pipe diameter size (here, from 4.52 to 7.5 cm). However, in pipes with diameters exceeding 7 cm, there is a reversal in the correlation of pipe diameter and erosion rate. Specifically, for pipe diameters of 8.52 to 10.52 cm, the impact is relatively slight; however, as the diameter further increases, the rate of erosion becomes constant, and pipe-wall erosion declining as pipe diameter increases.

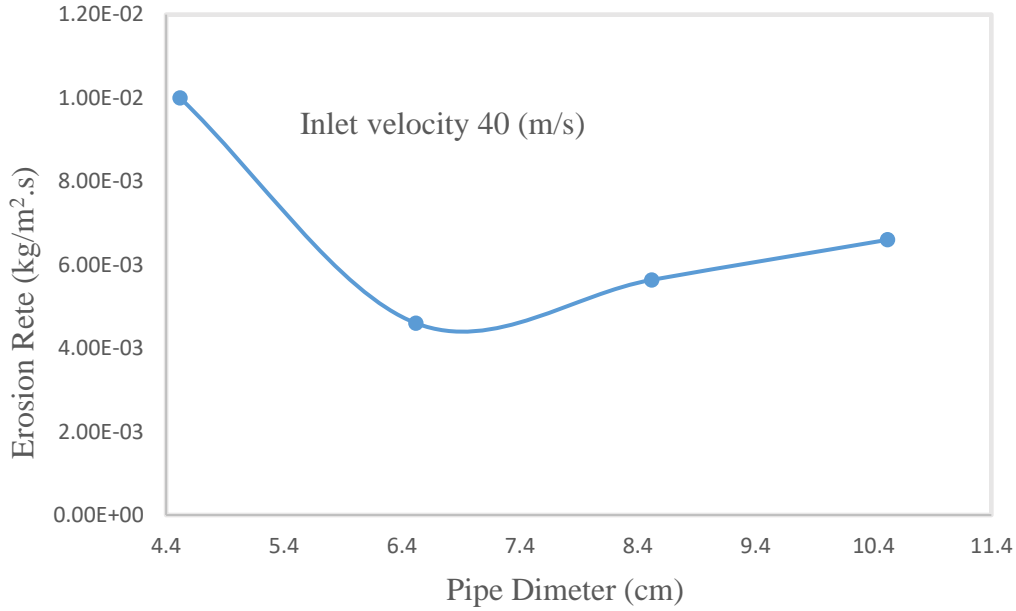


Fig. 4.11. Effect of pipe diameter on erosion rates at a velocity of 40 m/s and particle size of 200 (μm).

The mechanisms affecting carrier fluid viscosity and erosion rate are not well known. We use a model which posits the occurrence of pipeline erosion from various speeds and for particles of around 200 μm . The model also posits lower rates of erosion in pipelines when the viscosity is greater. Figure 4.12 charts the model for increasing levels of viscosity (from 9.29E^{-6} mPa.s to 1.37E^{-3} mPa.s). As can be seen in the figure, higher levels of viscosity result in higher rates of erosion. Researchers in [30] noted only slightly higher rates of erosion for 9.29E^{-6} mPa.s to 1.37E^{-3} mPa.s settings of increases in viscosity. The researchers suggested in [32] that both particle shape (e.g., spherical) and size played a role in their results.

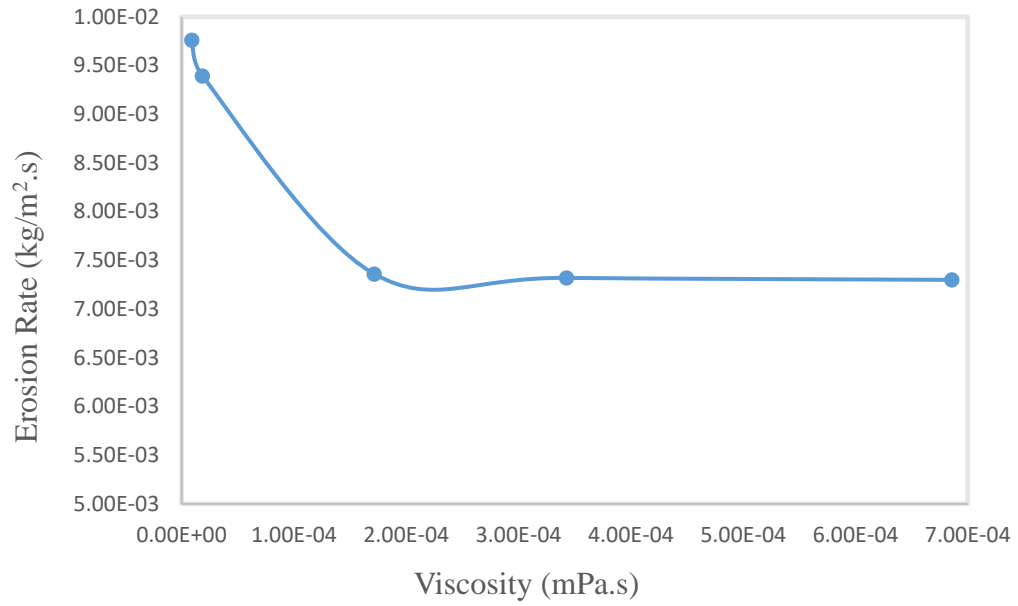


Fig. 4.12. Effect of viscosity on erosion rates at a velocity of 40 m/s and particle size of 200 (μm).

Conclusions

A CFD model combined with DPM was employed in this study as a means to measure and predict the flow erosion of particle-laden water. It was also used to measure and predict flow-induced displacement for relief pipeline downstream from bends. Simulations using a variety of factors (particle size, particle matter, velocity, carrier phase viscosity, pipe diameter, and total flow rate of the second phase) were performed using k-epsilon ($k-\epsilon$), k-omega ($k-\omega$) and (sst) turbulence models to measure the effects of factors such as inlet flow rates and pipe diameter. The results of the simulations led the researchers to support two key conclusions:

When determining a pipeline's distribution erosion or maximum number of erosions, the $k-\epsilon$ model performs better than the $k-\omega$ or sst models.

Erosion can increase according to particle diameter. Specifically, particle diameters of $10\ \mu\text{m}$ can result in erosion in excess of 70 to $100\ \mu\text{m}$ for velocities of 30 to $35\ \text{m/s}$.

Furthermore, due to the asymmetrical flow fields which occur in bends, there is an uneven fluid force impacting both the external and internal elbow walls, causing curve displacement in the pipes. Maximum displacement occurs near the outlet of the pipe, increasing in response to increased flow rates and/or decreased pipe diameter. The most extreme erosion areas are at elbows positioned downstream from bends, as this is the main impinging region for particles. Bigger rates of inlet flow lead to greater rates of erosion, but erosion rates can be mitigated by using larger pipe diameters.

References

- [1] H. K. Versteeg and W. Malalasekera, *An Introduction to Computational Fluid Dynamics - The Finite Volume Method*. 1995.
- [2] O. Paul and A. M. A. Mohames, "Erosion-Corrosion in Oil and Gas Industry: a Review," *Int. J. Metall. Mater.*, vol. 4, no. 3, pp. 7–28, 2014.
- [3] M. A. Islam and Z. N. Farhat, "Effect of impact angle and velocity on erosion of API X42 pipeline steel under high abrasive feed rate," *Wear*, vol. 311, no. 1–2, pp. 180–190, 2014.
- [4] E. Mahdi, A. Rauf, S. Ghani, A. El-Noamany, and A. Pakari, "Erosion-corrosion behavior and failure analysis of offshore steel tubular joint," *Int. J. Electrochem. Sci.*, vol. 8, no. 5, pp. 7187–7210, 2013.
- [5] M. Parsi, K. Najmi, F. Najafifard, S. Hassani, B. S. McLaury, and S. A. Shirazi, "A comprehensive review of solid particle erosion modeling for oil and gas wells and pipelines applications," *J. Nat. Gas Sci. Eng.*, vol. 21, pp. 850–873, 2014.
- [6] F. Mohammadi and J. Luo, "Effects of particle angular velocity and friction force on erosion enhanced corrosion of 304 stainless steel," *Corros. Sci.*, vol. 52, no. 9, pp. 2994–3001, 2010.
- [7] H. Zhu, J. Wang, B. Ba, Z. Wu, and W. Wang, "Numerical investigation of flow erosion and flow induced displacement of gas well relief line," *J. Loss Prev. Process Ind.*, vol. 37, pp. 19–32, 2015.
- [8] D. O. Njobuenwu and M. Fairweather, "Modelling of pipe bend erosion by dilute particle suspensions," *Comput. Chem. Eng.*, vol. 42, pp. 235–247, 2012.
- [9] J. C. Jo, D. G. Kang, and K. W. Roh, "Numerical Calculation of Shear Stress Distribution on the Inner Wall Surface of CANDU Reactor Feeder Pipe Conveying Two-Phase Coolant," *J. Press. Vessel Technol.*, vol. 131, no. 2, p. 021301, 2009.
- [10] S. Rinaldi, S. Prabhakar, S. Vengallatore, and M. P. Païdoussis, "Dynamics of microscale pipes containing internal fluid flow: Damping, frequency shift, and stability," *J. Sound Vib.*, vol. 329, no. 8, pp. 1081–1088, 2010.
- [11] F. Alijani and M. Amabili, "Nonlinear vibrations and multiple resonances of fluid filled arbitrary laminated circular cylindrical shells," *Compos. Struct.*, vol. 108, no. 1, pp. 951–962, 2014.

- [12] L. Wang, "Size-dependent vibration characteristics of fluid-conveying microtubes," *J. Fluids Struct.*, vol. 26, no. 4, pp. 675–684, 2010.
- [13] M. M. Zhang, J. Katz, and A. Prosperetti, "Enhancement of channel wall vibration due to acoustic excitation of an internal bubbly flow," *J. Fluids Struct.*, vol. 26, no. 6, pp. 994–1017, 2010.
- [14] M. M. Stack and S. M. Abdelrahman, "A CFD model of particle concentration effects on erosion-corrosion of Fe in aqueous conditions," *Wear*, vol. 273, no. 1, pp. 38–42, 2011.
- [15] Y. S. Tan *et al.*, "Tracking of data leaving the cloud," *Proc. 11th IEEE Int. Conf. Trust. Secur. Priv. Comput. Commun. Trust. - 11th IEEE Int. Conf. Ubiquitous Comput. Commun. IUCC-2012*, pp. 137–144, 2012.
- [16] H. Zhang *et al.*, "Numerical investigation of the location of maximum erosive wear damage in elbow: Effect of slurry velocity, bend orientation and angle of elbow," *Powder Technol.*, vol. 217, pp. 467–476, 2012.
- [17] L. Zeng, G. A. Zhang, and X. P. Guo, "Erosion-corrosion at different locations of X65 carbon steel elbow," *Corros. Sci.*, vol. 85, pp. 318–330, 2014.
- [18] M. Suzuki and M. Yamamoto, "Numerical Simulation of Sand Erosion Phenomena in a Single-Stage Axial Compressor," *J. Fluid Sci. Technol.*, vol. 6, no. 1, pp. 98–113, 2011.
- [19] R. Li, A. Yamaguchi, and H. Ninokata, "Computational Fluid Dynamics Study of Liquid Droplet Impingement Erosion in the Inner Wall of a Bent Pipe," *J. Power Energy Syst.*, vol. 4, no. 2, pp. 327–336, 2010.
- [20] Y. Zhang, E. P. Reuterfors, B. S. McLaury, S. A. Shirazi, and E. F. Rybicki, "Comparison of computed and measured particle velocities and erosion in water and air flows," *Wear*, vol. 263, no. 1–6 SPEC. ISS., pp. 330–338, 2007.
- [21] H. Zhu, Q. Pan, W. Zhang, G. Feng, and X. Li, "CFD simulations of flow erosion and flow-induced deformation of needle valve: Effects of operation, structure and fluid parameters," *Nucl. Eng. Des.*, vol. 273, pp. 396–411, 2014.
- [22] M. R. Sippola and W. W. Nazaroff, "Particle Deposition in Ventilation Ducts: Connectors, Bends and Developing Turbulent Flow," *Aerosol Sci. Technol.*, vol. 39, no. 2, pp. 139–150, 2005.
- [23] L. Jianzhong, S. Xing, and Y. Zhenjiang, "Effects of the aspect ratio on the sedimentation of a fiber in Newtonian fluids," *J. Aerosol Sci.*, vol. 34, no. 7, pp. 909–921, 2003.

- [24] M. Yu, M. Seipenbusch, M. Yu, A. J. Koivisto, and K. Hämeri, “Size Dependence of the Ratio of Aerosol Coagulation to Deposition Rates for Indoor Aerosols,” *Aerosol Sci. Technol.*, vol. 47, no. 4, pp. 427–434, 2013.
- [25] T. Sarver, A. Al-Qaraghuli, and L. L. Kazmerski, “A comprehensive review of the impact of dust on the use of solar energy: History, investigations, results, literature, and mitigation approaches,” *Renew. Sustain. Energy Rev.*, vol. 22, pp. 698–733, 2013.
- [26] K. Sun and L. Lu, “Particle flow behavior of distribution and deposition throughout 90° bends: Analysis of influencing factors,” *J. Aerosol Sci.*, vol. 65, pp. 26–41, 2013.
- [27] J. Lin, P. Lin, and H. Chen, “Research on the transport and deposition of nanoparticles in a rotating curved pipe,” *Phys. Fluids*, vol. 21, no. 12, pp. 1–11, 2009.
- [28] Y. Zhang, B. S. McLaury, and S. A. Shirazi, “Improvements of Particle Near-Wall Velocity and Erosion Predictions Using a Commercial CFD Code,” *J. Fluids Eng.*, vol. 131, no. 3, p. 031303, 2009.
- [29] S. Ke, L. Lin, and J. Hanhui, “Modeling and Numerical Analysis of the Solid Particle Erosion in Curved Ducts,” vol. 2013, 2013.
- [30] LEAP CFD Team, “Computational Fluid Dynamics (CFD) Blog - LEAP Australia & New Zealand | Tips & Tricks: Inflation Layer Meshing in ANSYS,” *LEAP Australia*, 2012. [Online]. Available: <https://www.computationalfluidynamics.com.au/tips-tricks-inflation-layer-meshing-in-ansys/>. [Accessed: 27-Jun-2018].
- [31] ANSYS, “ANSYS-In-text help.” 2017.
- [32] N. R. Kesana, S. A. Grubb, B. S. McLaury, and S. A. Shirazi, “Ultrasonic Measurement of Multiphase Flow Erosion Patterns in a Standard Elbow,” *J. Energy Resour. Technol.*, vol. 135, no. 3, p. 032905, 2013.
- [33] H. Arabnejad, A. Mansouri, S. A. Shirazi, and B. S. McLaury, “Abrasion erosion modeling in particulate flow,” *Wear*, vol. 376–377, no. November, pp. 1194–1199, 2017.
- [34] H. C. Meng and K. C. Ludema, “Wear models and predictive equations: their form and content,” *Wear*, vol. 181–183, no. PART 2, pp. 443–457, 1995.
- [35] X. Chen, B. S. McLaury, and S. A. Shirazi, “Numerical and experimental investigation of the relative erosion severity between plugged tees and elbows in dilute gas/solid two-phase flow,” *Wear*, vol. 261, no. 7–8, pp. 715–729, 2006.
- [36] J. Zhou, G. Liang, T. Deng, and J. Gong, “Route Optimization of Pipeline in Gas-Liquid

- Two-Phase Flow Based on Genetic Algorithm,” *Int. J. Chem. Eng.*, vol. 2017, 2017.
- [37] B. Bozzini, M. E. Ricotti, M. Boniardi, and C. Mele, “Evaluation of erosion-corrosion in multiphase flow via CFD and experimental analysis,” *Wear*, vol. 255, no. 1–6, pp. 237–245, 2003.